



Fractionation of O₂/N₂ and Ar/N₂ in the Antarctic ice sheet during bubble formation and bubble-clathrate hydrate transition from precise gas measurements of the Dome Fuji ice core

*Ikumi Oyabu¹, Kenji Kawamura^{1,2,3}, Tsutomu Uchida⁴, Shuji Fujita^{1,2}, Kyotaro Kitamura¹, Motohiro Hirabayashi¹, Shuji Aoki⁵, Shinji Morimoto⁵, Takakiyo Nakazawa⁵, Jeffrey P. Severinghaus⁶, Jacob Morgan⁶

¹ National Institute of Polar Research, Tokyo 190-8518, Japan

² Department of Polar Science, The Graduate University of Advanced Studies (SOKENDAI), Tokyo 190-8518, Japan

³ Japan Agency for Marine Science and Technology (JAMSTEC), Yokosuka 237-0061, Japan

10 ⁴ Division of Applied Physics, Faculty of Engineering, Hokkaido University, Sapporo 060-8628, Japan

⁵ Center for Atmospheric and Oceanic Studies, Graduate School of Science, Tohoku University, Sendai 980-8578, Japan

⁶ Scripps Institution of Oceanography, University of California San Diego, La Jolla, CA 92093, USA

Correspondence to: Ikumi Oyabu (oyabu.ikumi@nipr.ac.jp)

Abstract. The variations of $\delta\text{O}_2/\text{N}_2$ and $\delta\text{Ar}/\text{N}_2$ in the Dome Fuji ice core were measured from 112 m (bubbly ice) to 2001 m (clathrate hydrate ice) at high precision. Our method, combined with the low storage temperature of the samples (-50 °C), successfully excludes post-coring gas-loss fractionation signals from our data. From the bubbly ice to the middle of the bubble-clathrate transition zone (BCTZ) (112 – 800 m) and below the BCTZ (>1200 m), the $\delta\text{O}_2/\text{N}_2$ and $\delta\text{Ar}/\text{N}_2$ data exhibit orbital-scale variations similar to local summer insolation. The data in the lower BCTZ (800 – 1200 m) have large scatters, which may be caused by mm-scale inhomogeneity of air composition combined with finite sample lengths. The insolation signal originally recorded at the bubble close-off remains through the BCTZ, and the insolation signal may be reconstructed by analyzing long ice samples. In the clathrate hydrate zone, the scatters around the orbital-scale variability decrease with depth, indicating diffusive smoothing of $\delta\text{O}_2/\text{N}_2$ and $\delta\text{Ar}/\text{N}_2$. A simple gas diffusion model was used to reproduce the smoothing and thus constrain their permeation coefficients. The relationship between $\delta\text{Ar}/\text{N}_2$ and $\delta\text{O}_2/\text{N}_2$ is markedly different for the datasets representing bubble close-off (slope ~0.5), bubble-clathrate hydrate transformation (~1), and post-coring gas-loss (~0.2), suggesting that the contribution of the mass-independent and mass-dependent fractionation processes are different for those cases. The method and data presented here may be useful for improving the orbital dating of deep ice cores over the multiple glacial cycles and further studying non-insolation-driven signals (e.g., atmospheric composition) of these gases.

1 Introduction

Air trapped in polar ice sheets provides information on past climate and atmosphere. Air is transported mainly by molecular diffusion from the surface to the bottom of firn (typically 50 – 100 m below the snow surface) and trapped as air bubbles. During the bubble close-off process, relatively small gas molecules such as He, Ne, O₂ and Ar are preferentially excluded from



air bubbles to open pores (e.g., Bender et al., 1994a; Battle et al., 1996; Severinghaus and Battle, 2006; Huber et al., 2006). The size-dependent gas fractionation may be related to the size of channels within ice crystals (Huber et al., 2006) or the differences in the dominant diffusion mechanism (Ikeda-Fukazawa et al., 2004). Deep ice cores from Antarctic inland show $\delta\text{O}_2/\text{N}_2$ of -5 to -10 ‰ relative to the atmosphere due to the close-off fractionation (Bender, 2002; Suwa and Bender, 2008a, b; Kawamura et al., 2007; Extier et al., 2018). $\delta\text{Ar}/\text{N}_2$ has been rarely reported, and it is less depleted than $\delta\text{O}_2/\text{N}_2$ (Sowers et al., 1989; Bender et al., 1995; Severinghaus et al., 2009).

High correlations were found between local summer insolation and $\delta\text{O}_2/\text{N}_2$ records of the Vostok and Dome Fuji (DF) cores, which have been used for orbital dating of the cores (Bender, 2002; Suwa and Bender, 2008a; Kawamura et al., 2007). Summer insolation may influence the physical properties of snow, which later control the close-off fractionation (Bender, 2002; Kawamura et al., 2007; Fujita et al., 2009). The phasing between the local summer insolation and $\delta\text{O}_2/\text{N}_2$ signals and its variability are typically neglected in the dating practice. However, the $\delta\text{O}_2/\text{N}_2$ data from the EDC, Vostok and DF cores around the last interglacial period show discrepancies and high-frequency variabilities, challenging the assumption of stable phasing (Bazin et al., 2016).

The current understanding of the gas fractionation and hence the assessment of $\delta\text{O}_2/\text{N}_2$ and $\delta\text{Ar}/\text{N}_2$ as the local insolation proxy are hindered, at least partly, by the scarceness of the data that are unaffected by post-coring gas loss (during ice-core drilling and storage), which also fractionates $\delta\text{O}_2/\text{N}_2$ and $\delta\text{Ar}/\text{N}_2$ (Bender et al., 1995; Kawamura et al., 2007; Kobashi et al., 2008; Severinghaus et al., 2009; Sowers et al., 1989). For example, configurational diffusion may occur in microcracks to produce size-dependent and weak mass-dependent fractionations (Bender et al., 1995; Huber et al., 2006). Molecular diffusion through ice matrix may also produce size-dependent fractionation (Ikeda-Fukazawa et al., 2004). The DF, Vostok and GISP2 deep cores indeed showed gradual $\delta\text{O}_2/\text{N}_2$ depletion over several years at -25 – -35 °C (Kawamura et al., 2007; Suwa and Bender, 2008a, b).

Another obstacle to understanding the close-off fractionation lies in the transformation of bubbles to clathrate hydrates. In the bubble-clathrate hydrate transition zone (BCTZ: e.g., 450 – 1200 m at Dome Fuji, (Narita et al., 1999), extreme gas fractionations on the order of several 100 ‰ can occur between individual bubbles and clathrate hydrates due to lower dissociation pressure and larger permeation coefficient of O_2 relative to N_2 (e.g., Chazallon et al., 1998; Ikeda-Fukazawa et al., 2001). The microscopic gas fractionation, combined with the post-coring gas-loss fractionation, creates high variabilities of $\delta\text{O}_2/\text{N}_2$ and $\delta\text{Ar}/\text{N}_2$ from gas measurements in the BCTZ (Bender, 2002; Kawamura et al., 2007; Kobashi et al., 2008; Lüthi et al., 2010; Shackleton et al., 2019). Below the BCTZ, the variabilities of $\delta\text{O}_2/\text{N}_2$ and $\delta\text{Ar}/\text{N}_2$ decrease with depth over several hundred meters, possibly due to diffusive smoothing (Lüthi et al., 2010; Bereiter et al., 2014; Shackleton et al., 2019). The understanding of the smoothing process has been insufficient because of the lack of high-resolution gas data for a proper numerical simulation (Bereiter et al., 2014). Moreover, the fact that reliable $\delta\text{O}_2/\text{N}_2$ records have been available only from the



clathrate hydrate ice (i.e., older than ~100 kyr) has hindered the discussion of how the original close-off fractionation signals are preserved through the BCTZ.

A better understanding of the gas fractionation associated with bubble close-off and clathrate hydrate formation is important for the ice-core dating and eventual reconstruction of the past atmospheric ratios. Bereiter et al. (2009) predicted that the original gas composition is preserved in the inner part of the cores for a few decades at low temperature (e.g., -50 °C), based on a numerical simulation of gas diffusion. The prediction was verified by analyzing the DF core, which has been stored at -50 °C for ~20 years, after sufficiently removing its fractionated outer part (Oyabu et al., 2020). In this work, we employ the method by Oyabu et al. (2020) and measure $\delta\text{O}_2/\text{N}_2$ and $\delta\text{Ar}/\text{N}_2$ from the bubbly ice to clathrate hydrate ice in the DF core. In addition to the discrete sampling, we obtain high-resolution, continuous gas and chemical data at selected depth intervals to understand the smoothing process of $\delta\text{O}_2/\text{N}_2$ and $\delta\text{Ar}/\text{N}_2$ below the BCTZ. Moreover, the outer ice is also measured for discussing the artifactual fractionation during storage. We analyze the data mainly based on the relationships between $\delta\text{O}_2/\text{N}_2$, $\delta\text{Ar}/\text{N}_2$ and $\delta^{18}\text{O}$ of O_2 to distinguish the gas fractionation processes associated with the bubble close-off, transformation of bubbles to clathrate hydrates, and post-coring gas loss. A simple gas diffusion model is also employed to constrain the permeation coefficients of N_2 , O_2 and Ar, and discuss the preservation of insolation signals in the gas records through the BCTZ.

2 Methods

2.1 Ice core

We use the first Dome Fuji ice core (DF1 core) drilled from 1993 to 1997 (Watanabe et al., 2003). After transporting to Japan, the samples had been stored at -50 °C at the Institute for Low Temperature Science, Hokkaido University (until 2009) and the National Institute of Polar Research (NIPR, 2009 – present). Within the DF ice core, 105 – 450 m is bubbly ice, 450 – 1200 m is bubble-clathrate transition zone (BCTZ), and below 1200 m is bubble-free ice (Narita et al., 1999; Ohno et al., 2004).

2.2 Air extraction and measurements

A typical ice sample is ~60 g and ~110-mm long (corresponding to ~10 years) (Fig. 1a), which is cut out from a bulk section (~500-mm long). Because $\delta\text{O}_2/\text{N}_2$ and $\delta\text{Ar}/\text{N}_2$ near the sample surface are depleted by gas loss during storage, we removed the surface by more than 8 mm for clathrate ice (Oyabu et al., 2020) and 5 mm for bubbly ice (see below). For some samples in the BCTZ (1000 – 1200 m), we removed the surface by 20 mm (Fig. 1b) to minimize the signal of gas loss from high-pressure bubbles (Bender, 2002).

The thickness of surface removal (5 mm) for bubbly ice was determined as follows. Within a pair of samples with 3-mm removal, the sample with larger outer surface (“a2” in Fig. 1a) had generally lower $\delta\text{O}_2/\text{N}_2$ and $\delta\text{Ar}/\text{N}_2$, and slightly higher



$\delta^{18}\text{O}$ than the other sample (“a1” in Fig. 1a) (Fig. B1). No such tendency is observed with >5 mm surface removal (Fig. B1). We note that $\delta^{15}\text{N}$ is insensitive to the removal thickness (Fig. B1c), confirming its immunity from gas loss (Severinghaus et al., 2009; Oyabu et al., 2020).

100

The experimental procedures at NIPR are described elsewhere (Oyabu et al., 2020). Briefly, ice samples were evacuated for 2 hours and melted, and the released air was cryogenically collected into a sample tube. The air sample was split into two aliquots and measured with a mass spectrometer (Thermo DELTA V, for $\delta\text{O}_2/\text{N}_2$, $\delta\text{Ar}/\text{N}_2$, $\delta^{15}\text{N}$ and $\delta^{18}\text{O}$) and gas chromatographs (two Agilent 7890A, for CO_2 , CH_4 and N_2O concentrations; not shown in this study). Corrections were made for non-linearity of the elemental and isotopic ratios upon sample pressure, and for the dependency of $\delta^{15}\text{N}$, $\delta^{18}\text{O}$ and $\delta\text{Ar}/\text{N}_2$ upon $\delta\text{O}_2/\text{N}_2$ (Bender et al., 1994b). Then, the values were normalized to the modern atmosphere (Oyabu et al., 2020). Gravitational corrections were applied to $\delta\text{O}_2/\text{N}_2$, $\delta\text{Ar}/\text{N}_2$ and $\delta^{18}\text{O}$ using $\delta^{15}\text{N}$ of the same sample (Sowers et al., 1989). We measured 522 and 162 depths with single and replicates, respectively, between 112.88 to 2001.12 m (3 to 173 kyr BP).

105

110 We tested the possibility of gas loss during the sample evacuation (Craig et al., 1988). For a bubbly ice (446.4 m) and a clathrate hydrate ice (2001.1 m), we split each sample into five thin pieces of 13 – 18 g (Fig. 1d), and evacuated them for different durations (2 pieces for 20 minutes, 1 for 2 hours, and 2 for 5 hours). There are no dependence of $\delta\text{O}_2/\text{N}_2$, $\delta\text{Ar}/\text{N}_2$, $\delta^{15}\text{N}$ and $\delta^{18}\text{O}$ on the pumping time (Fig. B2). The bubbly ice data show somewhat low $\delta\text{O}_2/\text{N}_2$ and $\delta\text{Ar}/\text{N}_2$ for the 20-min evacuation, but the result is opposite to the expectation from gas loss. Also, larger variabilities of $\delta\text{O}_2/\text{N}_2$ and $\delta\text{Ar}/\text{N}_2$ are expected in the bubbly ice than in the clathrate hydrate ice (section 4.1). Thus, our method and core quality do not significantly fractionate the gases.

115

Eleven samples from 179.69 to 2496.55 m, stored for 11 years at -25 °C, were measured for $\delta\text{O}_2/\text{N}_2$ and $\delta^{15}\text{N}$ at Tohoku University. The analytical method was slightly modified from the previous method by Kawamura et al. (2007) as follows. The typical sample size was 250 g, and the measurements were made with a Delta plus XP (Thermo Fisher Scientific) with 64 changeover cycles. Analytical precisions (1σ) were estimated to be 0.4 and 0.011 ‰ for $\delta\text{O}_2/\text{N}_2$ and $\delta^{15}\text{N}$, respectively.

120

2.3 High-resolution analyses

The air composition and ion concentrations were measured on five 50-cm segments at the resolutions of 1 – 2 cm. Three segments were measured for the air (1258.51 – 1258.99 m, 1389.79 – 1390.32 m and 1893.51 – 1893.99 m), and two segments were measured for the air and ions (1292.29 – 1292.82 m and 1399.03 – 1399.48 m). In Fig. 1c, the X and Y sections were divided into 25- and 12.5-mm pieces for air and ion measurements, respectively.

125



130 For the ion measurements, the ice was decontaminated by shaving-off by ~ 3 mm, and then chopped off with a ceramic knife and sampled in particle-free plastic bags. They were melted in a clean laboratory (class 10,000) and analyzed for the concentrations of Cl^- , SO_4^{2-} , NO_3^- , F^- , CH_3SO_3^- , Na^+ , NH_4^+ , K^+ , Mg^{2+} and Ca^{2+} using ion chromatography (Thermo Fisher Scientific Dionex ICS-5000+) (Goto-Azuma et al., 2019).

2.4 Diffusion model

135 We simulate diffusive smoothing of $\delta\text{O}_2/\text{N}_2$ and $\delta\text{Ar}/\text{N}_2$ in the clathrate hydrate ice with a one-dimensional diffusion model (Ikeda-Fukazawa et al., 2005; Bereiter et al., 2009; Bereiter et al., 2014). The model assumes that the molecular diffusion through ice lattice is driven by the concentration gradient of gas molecules dissolved in ice, which are in equilibrium with clathrate hydrates in respective layers of the model. Permeabilities of O_2 and N_2 are poorly known, thus we used three sets of model-based permeabilities estimated by Ikeda-Fukazawa et al. (2001) (hereafter IkFk01), Salamatin et al. (2001) (hereafter Salm01), and Ikeda-Fukazawa et al. (2005) (hereafter IkFk05) (Fig. 2, Table A2, A3).

There are no published permeability of Ar in ice, thus we used two formulations proposed by Kobashi et al. (2015) (Fig. 2). The first permeability $k_{Ar(I)}$ uses diffusion coefficients of N_2 , O_2 and Ar at 270 K from the molecular dynamics simulations by Ikeda-Fukazawa et al. (2004) ($D_{\text{N}_2}^{270}$: $2.1 \times 10^{-11} \text{ m}^2 \text{ s}^{-1}$, $D_{\text{O}_2}^{270}$: $4.7 \times 10^{-11} \text{ m}^2 \text{ s}^{-1}$ and D_{Ar}^{270} : $4.0 \times 10^{-11} \text{ m}^2 \text{ s}^{-1}$):

$$145 \quad k_{Ar(I)} = k_{O_2} - \left(\frac{D_{O_2}^{270} - D_{Ar}^{270}}{D_{O_2}^{270} - D_{N_2}^{270}} \right) (k_{O_2} - k_{N_2}). \quad (1)$$

The second permeability $k_{Ar(II)}$ is based on the observations that $\delta\text{Ar}/\text{N}_2$ is often depleted about half of $\delta\text{O}_2/\text{N}_2$ (e.g., Severinghaus et al., 2009), and is given by:

$$k_{Ar(II)} = \frac{(k_{N_2} + k_{O_2})}{2}. \quad (2)$$

150 To take into account the actual ice sheet condition, the temperature and grid size were revised every ~ 100 model-years according to the temperature and thinning function. Initial depth profiles of $\delta\text{O}_2/\text{N}_2$ and $\delta\text{Ar}/\text{N}_2$ were constructed by repeating the 50-cm segment of the 2.5-cm continuous data at 1258 m (81.7 kyr BP) (Fig. 6). We run the model from 1258 to 2000 m (for ~ 100 kyr) to cover the depth range of our data. Further details of the model are described in Appendix A.

3 Results

3.1 $\delta\text{O}_2/\text{N}_2$ and $\delta\text{Ar}/\text{N}_2$ in bubbly ice, BCTZ ice and clathrate-hydrate ice

155 $\delta\text{O}_2/\text{N}_2$ and $\delta\text{Ar}/\text{N}_2$ from the 11-cm samples are shown in Figure 3b and 3c. As expected, most data are negative (i.e., lower than the atmosphere) because of preferential loss of O_2 and Ar relative to N_2 during bubble close-off (Bender et al., 1995;



Severinghaus and Battle, 2006). The average values of $\delta\text{O}_2/\text{N}_2$ and $\delta\text{Ar}/\text{N}_2$ are about -10 and -5 ‰, with the overall ranges of -14 to -5 and -7 to -3 ‰, respectively.

- 160 Variations in $\delta\text{O}_2/\text{N}_2$ and $\delta\text{Ar}/\text{N}_2$ for the depths shallower than ~800 m and deeper than ~1200 m have similarity with local summer insolation curve, while little similarity is found for 800 – 1200 m with extremely large scatters (Fig. 4). We assess the scatters in the data by taking residuals of $\delta\text{O}_2/\text{N}_2$ and $\delta\text{Ar}/\text{N}_2$ from their low-pass filtered curves (Fig. 3d and 3e). The average residuals of $\delta\text{O}_2/\text{N}_2$ are 1.1 ‰ in the bubbly ice zone (~112 – 450 m), 0.7 ‰ in the upper BCTZ (~450 – 800 m), 4.6 ‰ in the lower BCTZ (800 – 1200 m), 2.3 ‰ just below BCTZ (~1200 – 1480 m), and 0.4 ‰ in the deeper depths (~1480 – 2000 m).
- 165 The average residuals of $\delta\text{Ar}/\text{N}_2$ also show similar pattern (0.5 ‰ for 112 – 450 m, 0.5 ‰ for 450 – 800m, 2.8 ‰ for 800 – 1200 m, 1.3 ‰ for 1200 – 1480 m, and 0.3 ‰ for ~1480 – 2000 m). Below, we divide our dataset into four depth ranges guided by the scatters as well as the classic boundaries between bubbly ice zone, BCTZ and clathrate ice zone (Narita et al., 1999; Ohno et al., 2004).

170 3.1.1 112 – 450 m (bubbly ice)

- The average $\delta\text{O}_2/\text{N}_2$ and $\delta\text{Ar}/\text{N}_2$ are -10.9 and -5.6 ‰, with the overall ranges of -13.0 to -7.0 and -7.2 to -3.4 ‰, respectively. Figs. 2f and 2g show differences of $\delta\text{O}_2/\text{N}_2$ and $\delta\text{Ar}/\text{N}_2$ between ice samples cut from the same depth (Fig. 1a) (hereafter referred to as pair difference or $\Delta\delta\text{O}_2/\text{N}_2$ and $\Delta\delta\text{Ar}/\text{N}_2$). Ranges of $\Delta\delta\text{O}_2/\text{N}_2$ and $\Delta\delta\text{Ar}/\text{N}_2$ are ~0.02 to 0.97 ‰ and 0.01 to 0.96 ‰, respectively. Pair differences are usually used to calculate the pooled standard deviation, a metric of analytical
- 175 precision. Instead, we use it to evaluate spatial variability in air composition for a given depth in the ice sheet (pair differences of $\delta^{15}\text{N}$ and $\delta^{18}\text{O}$ are plotted in Fig. B3 and pooled standard deviations are summarized in Table C1).

- Our new $\delta\text{O}_2/\text{N}_2$ data are compared with previously obtained data at Tohoku University using the samples stored at -25 °C for various durations (Fig. 5). As expected, the samples stored at -25 °C generally show lower $\delta\text{O}_2/\text{N}_2$ than those stored at -50 °C,
- 180 with dependency on the storage duration. Also, while the data from the -50 °C samples slightly increase with depth in the bubbly ice zone as expected from the insolation variation, the data from the -25 °C samples tend to decrease with depth possibly due to the increase in bubble pressure (leading to larger gas-loss) (Ikeda-Fukazawa et al., 2005; Kawamura et al., 2007).

3.1.2 450 – 800 m (upper BCTZ)

- 185 The number and size of clathrate hydrates gradually increase with depth, but air bubbles are still the dominant form of air inclusion (Fig. 3i, 3j) (Ohno et al., 2004). In the lowermost part of this range (below 720 m), clathrate hydrates with extremely enriched $\delta\text{O}_2/\text{N}_2$ (> ~1000 ‰) are found by Raman spectroscopy (Fig. 3h) (Ikeda-Fukazawa et al., 2001). The $\delta\text{O}_2/\text{N}_2$ and



190 $\delta\text{Ar}/\text{N}_2$ values from the gas analyses smoothly connect with those in the bubbly ice zone, with a slightly increasing trend with depth (Fig. 3b, 3c). The pair differences of $\delta\text{O}_2/\text{N}_2$ and $\delta\text{Ar}/\text{N}_2$ are smaller than 1 ‰ until ~650 m, below which they show high values (> 3 ‰, Fig. 3f, 3g).

3.1.3 800 – 1200 m (lower BCTZ)

Major transition from air bubbles to clathrate hydrates occur in this depth range (Fig. 3i, 3j) (Ohno et al., 2004). The $\delta\text{O}_2/\text{N}_2$ values of clathrate hydrates decrease from extremely high values towards the atmospheric value, and those of remaining air bubbles decrease to extremely negative values (~ -500 ‰) (Fig. 3h) (Ikeda-Fukazawa et al., 2001).

200 In contrast to the upper BCTZ, the bulk $\delta\text{O}_2/\text{N}_2$ and $\delta\text{Ar}/\text{N}_2$ in the lower BCTZ show elevated scatters (Fig. 3b-e). Very high $\delta\text{O}_2/\text{N}_2$ scatters have also been reported from the Vostok (Suwa and Bender, 2008a), GISP2 (Kobashi et al., 2008) and WAIS Divide (Shackleton et al., 2019) ice cores, with numerous positive values (higher than the atmosphere). The previous data were affected by the post-coring gas loss, thus they were interpreted only as artifacts created by the preferential gas loss from extremely N_2 -rich air bubbles (Bender, 2002; Ikeda-Fukazawa et al., 2001; Kobashi et al., 2008; Shackleton et al., 2019). In our data, relatively few samples (six and ten samples for $\delta\text{O}_2/\text{N}_2$ and $\delta\text{Ar}/\text{N}_2$, respectively) show positive values, and even the samples with twice the surface removal (20 mm) show large scatters. Thus, the large $\delta\text{O}_2/\text{N}_2$ and $\delta\text{Ar}/\text{N}_2$ variabilities naturally occur in this zone. The pair differences of $\delta\text{O}_2/\text{N}_2$ and $\delta\text{Ar}/\text{N}_2$ are also large (up to ~10 ‰, Fig. 3g, 3h; Table C1), indicating large inhomogeneities also in the horizontal direction.

3.1.4 1200 – 1980 m (clathrate hydrate ice)

210 Between 1200 and 1480 m, the $\delta\text{O}_2/\text{N}_2$ and $\delta\text{Ar}/\text{N}_2$ data show smaller scatters than those in the lower BCTZ (Fig. 3b-e), and their low-pass filtered curves (corresponding to ~80 to 100 kyr BP) show similarity to the local summer insolation (Fig. 4). The residuals of the data from the filtered curves are up to ~5 and ~3 ‰ for $\delta\text{O}_2/\text{N}_2$ and $\delta\text{Ar}/\text{N}_2$, respectively. The large scatters below the BCTZ have also been found in the WAIS Divide (Shackleton et al., 2019), EDML and EDC (Lüthi et al., 2010) ice cores. The pair differences of $\delta\text{O}_2/\text{N}_2$ and $\delta\text{Ar}/\text{N}_2$ are 1 – 2 ‰ just below the BCTZ (~1200 m), and they decrease with depth to < 0.1 ‰ (Fig. 3f, 3g, Table C1).

215 Below 1480 m, the $\delta\text{O}_2/\text{N}_2$ and $\delta\text{Ar}/\text{N}_2$ variations show remarkable similarities with the local summer insolation with small scatters (Fig. 4). The pair differences are also small (Fig. 3f, 3g, Table C1). The previous $\delta\text{O}_2/\text{N}_2$ data corrected for the gas-loss fractionation (measured at Tohoku University; Kawamura et al., 2007) agree well with our new data (Fig. 5), suggesting that the inner part of the ice core stored at -50 °C has kept the original $\delta\text{O}_2/\text{N}_2$ for two decades.



220 3.2 Outer ice

In almost all outer ice samples, $\delta\text{O}_2/\text{N}_2$ and $\delta\text{Ar}/\text{N}_2$ are significantly lower and $\delta^{18}\text{O}$ is significantly higher than those in the inner ice, as expected for gas loss (Ikeda-Fukazawa et al., 2005; Severinghaus et al., 2009). The outer ice stored at -30°C for ~ 1 year shows larger gas-loss signals than those stored at -50°C (Fig. B4), indicating that the gas-loss fractionation strongly depends on the storage temperature and duration. In the lower BCTZ, some $\delta\text{O}_2/\text{N}_2$ and $\delta\text{Ar}/\text{N}_2$ values from the outer ice are positive (Fig. B4a, B4b), possibly due to the preferential gas loss from N_2 -rich bubbles (Bender et al., 1995). We do not find significant differences between the outer and inner pieces for $\delta^{15}\text{N}$, CH_4 concentration and N_2O concentration (Fig. B4d – f). The results are consistent with the earlier notion that only the molecules smaller than 3.6 \AA in collision diameter (O_2 and Ar among the above species) significantly fractionate (Huber et al., 2006; Severinghaus and Battle, 2006).

230 3.3 High-resolution data

The high-resolution data ($\sim 1258, 1292, 1390, 1399$ and 1894 m) are shown in Figure 6. For the upper four depths, $\delta\text{O}_2/\text{N}_2$ and $\delta\text{Ar}/\text{N}_2$ fluctuate with very large amplitudes (peak-to-peak: $10 - 30 \text{ ‰}$) and the cycles of $10 - 15 \text{ cm}$. In the deepest sample (1894 m), the values are quite stable. The standard deviations of $\delta\text{O}_2/\text{N}_2$ are $8.4, 5.9, 5.8, 3.1$ and 0.2 ‰ , and those of $\delta\text{Ar}/\text{N}_2$ are $12.5, 6.4, 5.6, 3.4$ and 0.2 ‰ for $1258, 1292, 1390, 1399$ and 1894 m , respectively.

The data are averaged over 4 to 5 consecutive samples and compared with the data from the normal (11 cm) samples (Fig. 6). Two normal samples at ~ 1293 and 1390 m are taken from the same depths as the high-resolution measurements, and they agree with the averages of the high-resolution data. The standard deviation of the averaged data (blue curves in Fig. 6) for the upper four depths are 1.4 to 2.8 ‰ for $\delta\text{O}_2/\text{N}_2$ and 0.8 to 1.5 ‰ for $\delta\text{Ar}/\text{N}_2$, which are significantly higher than that for the deepest sample (0.1 and 0.2 ‰). High variabilities at 10-cm scales have also been found in the continuous measurements of the GRIP core (in the BCTZ, Huber and Leuenberger, 2004) and EDML core (just below the BCTZ, Lüthi et al., 2010). Also, in the GRIP data, the variabilities of $\delta\text{O}_2/\text{N}_2$ well below the BCTZ ($\sim 2500\text{-m}$ depth) are much smaller than those in the lower BCTZ ($\sim 1100 - 1400 \text{ m}$) (Huber and Leuenberger, 2004).

Major ion concentrations ($\text{Na}^+, \text{Mg}^{2+}, \text{Ca}^{2+}, \text{Cl}^-, \text{SO}_4^{2-}$ and NO_3^-) at 12.5-mm resolution from the two depths (1258 and 1399 m) are shown in Figure 7. The $\text{Na}^+, \text{Mg}^{2+}$ and Ca^{2+} concentrations show similar variations, and they appear to be correlated with the gas records. For example, narrow dips in the ion concentrations at $1258.88 - 1258.89$ and $1258.94 - 1258.95 \text{ m}$ possibly correspond to the dips in the gas records. Another example is common dips in the $\text{Na}^+, \text{Mg}^{2+}, \text{Ca}^{2+}, \text{Cl}^-$, and SO_4^{2-} concentrations and the gas data for $1399.17 - 1399.18 \text{ m}$. On the other hand, the $\text{Cl}^-, \text{SO}_4^{2-}$ and NO_3^- concentrations show



250 smooth variations possibly due to their higher mobility in firn and ice. The correlation coefficients between the ion concentrations and gas ratios are summarized in Table 1. For calculating the correlation coefficients, the ion data are resampled to the depths of the gas data. Significant correlations with the gas data are found for the Na^+ , Mg^{2+} and Ca^{2+} concentrations.

4 Discussion

4.1 Fractionation in firn

255 The $\delta\text{O}_2/\text{N}_2$ and $\delta\text{Ar}/\text{N}_2$ data for the bubbly ice, upper BCTZ and below BCTZ show variations similar to the local summer insolation (Fig. 4). For the first time, we find the insolation signals in the top part of the ice sheet, supporting the link between the local summer insolation and close-off fractionation through the effects on the snow metamorphism (Bender, 2002; Fujita et al., 2009).

260 In the bubbly ice zone, the scatters of the data are significantly larger than those of the pair differences, probably reflecting high variabilities of natural close-off fractionation in the vertical direction. In the Dome Fuji region, firn layerings of several 10 cm are found in $\delta^{18}\text{O}$ of ice, ion concentrations and density (Hoshina et al., 2014; Fujita et al., 2016). The layers closed-off deeper may be less depleted in O_2 and Ar because (1) air bubbles spend a shorter time in the close-off zone, and (2) $\delta\text{O}_2/\text{N}_2$ and $\delta\text{Ar}/\text{N}_2$ are enriched deeper in the open pores (e.g., Severinghaus and Battle, 2006). Also, microbubbles may form near
265 the surface (Lipenkov, 2000) and become extremely depleted in O_2 and Ar (Ohno et al., 2021), also causing the $\delta\text{O}_2/\text{N}_2$ and $\delta\text{Ar}/\text{N}_2$ variations (Kobashi et al., 2015). Hereafter, we collectively call the natural fractionation during the firn densification and bubble formation as “close-off fractionation”.

As discussed above, the relationship between $\delta\text{Ar}/\text{N}_2$ and $\delta\text{O}_2/\text{N}_2$ (after gravitational correction using $\delta^{15}\text{N}$) in our data is
270 expected only to reflect natural fractionations. For bubbly ice, we find a high correlation between $\delta\text{Ar}/\text{N}_2$ and $\delta\text{O}_2/\text{N}_2$ with the slope of 0.50 ± 0.01 (Fig. 8, Table C2), which agrees with that of pair differences (0.53 ± 0.04) (Fig. 9, Table C2). The smaller fractionation for $\delta\text{Ar}/\text{N}_2$ is consistent with the size-dependent fractionation. We find similar slopes in the upper BCTZ, lower BCTZ and below the BCTZ (0.45 ± 0.01 , 0.61 ± 0.01 , 0.42 ± 0.02 , respectively, Table C2), despite large scatters in the lower BCTZ and just below the BCTZ (~800 – 1480 m). We interpret the similarity of the slopes as preservation of the close-off
275 fractionation signals through the BCTZ. The slight differences between the slopes in the different zones might arise from different temperature or accumulation rate in the past (affecting the close-off fractionation), or natural variations of O_2 in the atmosphere.

A firn-air study at WAIS Divide (Battle et al., 2011) provided the evidence of mass-dependent fractionation associated with
280 the close-off process with the slope of $\delta^{18}\text{O}$ vs. $\delta\text{O}_2/\text{N}_2$ of -0.0090 (‰ / ‰). For the DF ice-core data, the pair differences in the bubbly ice zone (Fig. B5), as well as the data for the last 2000 years (Oyabu et al., 2020) do not show significant correlations



between $\delta^{18}\text{O}$ and $\delta\text{O}_2/\text{N}_2$. Thus, our data cannot verify the mass-dependent fractionation, and much higher precision is required to detect the $\delta^{18}\text{O}$ change of ~ 0.01 ‰ expected for the range of DF $\delta\text{O}_2/\text{N}_2$.

285 From the comparison of three Antarctic inland cores (EDC, Vostok, DF) that showed large short-term $\delta\text{O}_2/\text{N}_2$ variabilities and discrepancies between the cores around the last interglacial period, Bazin et al. (2016) discussed the possibility of non-orbital-scale variabilities of close-off fractionation. In our data, the residuals of $\delta\text{O}_2/\text{N}_2$ from the filtered curve are small ($1\sigma = \sim 0.5$ ‰) below ~ 1480 m (Fig. 3d), whereas the previous data (after gas-loss correction) show the variability of 1.3 ‰ for the similar depth range (Kawamura et al., 2007) (Fig. 5). Thus, the large short-term variabilities in the previous datasets may be mostly
290 attributed to the poor ice core quality, and the actual short-term variability of close-off fractionation may be rather small, at least for the DF core.

4.2 Bubble-clathrate transformation fractionation

In the upper BCTZ, the residuals of $\delta\text{O}_2/\text{N}_2$ and $\delta\text{Ar}/\text{N}_2$ from the low-pass filtered curves exhibit scatters of ~ 3 ‰ and ~ 2 ‰
295 (peak-to-peak), respectively, which are much smaller than those in the lower BCTZ (Fig. 4). Pair differences are similar to those at the bottom of the bubbly ice zone, suggesting insignificant effects of the clathrate hydrate formation on the measured $\delta\text{O}_2/\text{N}_2$ and $\delta\text{Ar}/\text{N}_2$ until ~ 40 % of air bubbles are transformed to clathrate hydrates. This may be reasonably explained by the dominance of direct conversion of air bubbles to clathrate hydrates (thus little displacements of molecules) in the early stages of bubble-clathrate transformation (Lipenkov, 2000). It may also be the case that the distance of gas diffusion from the bubbles
300 to clathrate hydrates, even if it occurs, is too short to create scatters in the bulk $\delta\text{O}_2/\text{N}_2$ and $\delta\text{Ar}/\text{N}_2$.

In the lower BCTZ, the scatters around the orbital scale variations dramatically increase for $\delta\text{O}_2/\text{N}_2$ and $\delta\text{Ar}/\text{N}_2$ despite the sufficient removal of the outer ice (Fig. 3, 4). Microscopic observations by Ohno et al. (2004) found layered distributions of air bubbles and clathrate hydrates in the lower BCTZ, as well as high spatial variability of total number of air inclusions on a
305 few mm-scales, possibly due to diminishing bubbles by transferring their molecules to nearby clathrates. Using their number concentrations of air bubbles and clathrate hydrates, the average distance between air inclusions is estimated to be 1.1 mm. Thus, the distance of air migration associated with the bubble-clathrate transformation should be on this order. Ikeda-Fukazawa et al. (2001) observed extremely fractionated bubbles and clathrate hydrates in the lower BCTZ, up to about +1000 ‰ for clathrate hydrates and -740 ‰ for bubbles for $\delta\text{O}_2/\text{N}_2$. From these observations, we suggest that the highly fractionated bubbles
310 and clathrate hydrates may be stratified in mm-scale layers, and that the scatters in our dataset may be produced by random inclusion of such fractionated layers at the top and/or bottom of the ice samples.



The slopes of $\delta\text{Ar}/\text{N}_2$ vs. $\delta\text{O}_2/\text{N}_2$ from the pair differences are close to 1 for both the upper and lower BCTZ (Fig. 9c and 9d, Table C2). They are strikingly different from the that in the bubbly ice (Fig. 9b, Table C2) and should be created by the fractionations associated with bubble-clathrate transition, because the amplitudes of $\Delta\delta\text{O}_2/\text{N}_2$ and $\Delta\delta\text{Ar}/\text{N}_2$ are larger than those in the bubbly ice by an order of magnitude. We also investigate the pair differences of $\delta^{18}\text{O}$ vs. $\delta\text{O}_2/\text{N}_2$, which may be an indicator of mass-dependent fractionation. We find no correlation between $\Delta\delta^{18}\text{O}$ and $\Delta\delta\text{O}_2/\text{N}_2$ with relatively wide ranges of $\Delta\delta\text{O}_2/\text{N}_2$ (up to 10 ‰, Fig. B5), indicating that the fractionation by the bubble-clathrate transformation is not mass-dependent. This is clearly different from the known correlations between $\Delta\delta^{18}\text{O}$ and $\Delta\delta\text{O}_2/\text{N}_2$ for bubble close-off (Battle et al., 2011) and post-coring gas loss (Severinghaus et al., 2009). Thus, we suggest that the net fractionation associated with the bubble-clathrate transformation and molecular diffusion between air inclusions within the ice sheet is mass-independent, and that the bubble close-off and post-coring gas-loss fractionations include mass-dependent processes for molecules smaller than 3.6 Å such as He, O₂ and Ar (Craig and Scarsi, 1997; Severinghaus et al., 2009). For the BCTZ, the slower permeation of Ar than that of O₂ may be counteracted by the lower dissociation pressure of Ar than O₂, which should produce a steeper Ar partial pressure gradient from the bubbles to the growing clathrate. This hypothesis may explain the observed similarity of $\delta\text{Ar}/\text{N}_2$ and $\delta\text{O}_2/\text{N}_2$ enrichment in clathrates. For the bubble close-off, such a cancellation cannot occur, explaining the observed $\delta\text{Ar}/\text{N}_2$ that is only half as enriched as $\delta\text{O}_2/\text{N}_2$. Instead, the bubble close-off fractionation of small molecules (<3.6 Å molecular diameter) appears to be caused by permeation through the thin ice wall of freshly-formed bubbles via both the bond-breaking mechanism (mass-independent) and the interstitial mechanism (mass-dependent; Ikeda-Fukazawa et al., 2004; Severinghaus and Battle, 2006; Battle et al., 2011).

We find similar slopes (~ 1) of $\Delta\delta\text{Ar}/\text{N}_2$ vs. $\Delta\delta\text{O}_2/\text{N}_2$ in the BCTZ of the WAIS Divide (Seltzer et al., 2017) and South Pole (Severinghaus, 2019) ice cores, although the samples have possibly experienced post-coring gas loss to some extent (Table C2). The fact that the different cores from a wide range of temperature show similar relationships between $\Delta\delta\text{Ar}/\text{N}_2$ and $\Delta\delta\text{O}_2/\text{N}_2$ may suggest that the permeation coefficients of O₂ and Ar in ice have similar dependence on temperature.

4.3 Preservation of insolation signal through BCTZ

Below the BCTZ, the low-pass filtered $\delta\text{O}_2/\text{N}_2$ and $\delta\text{Ar}/\text{N}_2$ show close resemblance to the variations of local summer insolation, although the residuals are rather scattered until 1480 m (Fig. 3, 4). The large scatters probably originate in the extreme layered fractionation in the lower BCTZ. Until the conversion of bubbles to clathrate hydrates complete (at ~ 1200 m), gas flux from the remaining (extremely fractionated) bubbles to clathrate hydrates should continue and enhance the inhomogeneity of gas composition. Once all bubbles disappear, the gas flux occurs only between clathrate hydrates; thus, their compositions become gradually homogenized. The major homogenization finishes within 300 m (25,000 years) below the BCTZ, and further



345 homogenization continues to ~500 m (~50,000 years) below the BCTZ where the scatters become small and stable (± 0.2 ‰)
(Fig. 3d, 3e and 12).

350 In contrast to the scatters from the 11-cm samples discussed above, the pair differences decrease sharply at the bottom of
BCTZ (Fig. 3f, 3g), suggesting smaller spatial variability of gas composition in the horizontal direction. The 2.5-cm continuous
data from the four 50-cm samples (1258 to 1399 m) also show much higher variabilities (5 - 10 ‰ difference between
neighboring samples) than the pair differences (Fig. 3f, 3g and 6). Thus, our data consistently show the large anisotropy of gas
fractionation, as expected from the layered clathrate hydrate formation in the BCTZ (Ohno et al., 2004). The positive
correlations between the gas ratios and Na^+ , Mg^{2+} and Ca^{2+} concentrations are consistent with the suggestion by Ohno et al.
(2010) that nucleation of clathrate hydrates tends to occur in the layers with abundant micro-inclusions, because the elements
Na, Mg and Ca likely exist as water-soluble salts (Oyabu et al., 2014 and references therein). Thus, the high-micro-inclusion
layers may attract O_2 and Ar from air bubbles in the adjacent layers with fewer micro-inclusions. The same conclusion was
355 reached by Huber and Leuenberger (2004) (albeit with ~50 times larger measurement uncertainties than ours), based on the
quasi-annual cycles in the $\delta\text{O}_2/\text{N}_2$ and $\delta\text{Ar}/\text{N}_2$ in the GRIP ice core, Greenland, and their similarity with Ca^{2+} concentrations.

360 The molecular diffusivities should depend on the direction in the ice sheet and also contribute to the horizontal homogeneity.
The c-axes orientation gradually becomes clustered around the vertical, and the crystal grains become horizontally elongated,
by the vertical compression within the ice sheet (Azuma et al., 2000). In terms of molecular diffusion through ice matrix, the
diffusivity in the direction perpendicular to the c-axis is greater than that in the direction parallel to the c-axis (Ikeda-Fukazawa
et al., 2004). For the diffusion along grain boundaries, the pathway should be shorter in the horizontal direction due to the
crystal elongation. In addition, lattice defect and dislocation within ice crystals tend to develop along the basal plane (Hondoh,
365 2009), possibly providing another pathway for gas diffusion. All these mechanisms should contribute to preferential
homogenization of gases in the horizontal direction.

370 The results of the diffusion model for 2.9, 13.7, 14.5 and 67.5 kyr (at 1292, 1390, 1399 and 1894 m, respectively) after the
initial state (81.7 kyr BP at 1258 m, Fig. 6) are resampled at 2.5-cm intervals and compared with the data (Fig. 10). The IkFk05
permeation parameters give the smoothest $\delta\text{O}_2/\text{N}_2$ profiles with a poor agreement with the data (Fig. 10c). The IkFk01
parameters produce the profiles similar to the data at 1292 m, but the model results are too smooth at 1390 and 1399 m (Fig.
10b). The results with the Salm01 parameters agree well with the data, including rapid changes (>10 ‰) within a few
consecutive samples and the standard deviation (~3 ‰) at 1399 m (Fig. 10a). We note that the data at 1390 and 1399 m show
rather different standard deviations (5.8 and 3.1 ‰) probably reflecting the original fractionations in the BCTZ. Thus, the
375 model-data comparison is inadequate with the small number of cases. For Ar, the model results with the scaling function Ar(II)
are closer to the data than those with Ar(I) (Fig. 11).



380 The standard deviations of the model results resampled at 11-cm intervals are compared with the residual $\delta\text{O}_2/\text{N}_2$ and $\delta\text{Ar}/\text{N}_2$ data from the low-pass filtered curves (Fig. 12) (following Bereiter et al., 2014). Exponential fitting curves through the residual data (black line) are in close agreements with the model results with the Salm01 and Ar(II) permeation parameters. On the other hand, the model results with the other parameters (IkFk01, IkFk05 and Ar(I)) show too rapid decrease in comparison with the data. Therefore, our datasets (high-resolution and normal datasets) consistently support the Salm01 and Ar(II) permeation parameters at around 240 K (temperature at DF for the simulated depths).

385 From the Salm01 parameters, the rate of diffusive migration is on the order of 0.1 mm per 10 kyr (10^{-10} m s⁻¹). Therefore, we favor the interpretation that the extreme scatter of $\delta\text{O}_2/\text{N}_2$ and $\delta\text{Ar}/\text{N}_2$ in the BCTZ in our datasets are caused by mm-scale inhomogeneity of the compositions of air inclusions combined with the finite sample length, rather than by cm-scale migration of gas molecules. We also suggest that the original insolation signal on $\delta\text{O}_2/\text{N}_2$ and $\delta\text{Ar}/\text{N}_2$ in the BCTZ may be reconstructed by analyzing long ice samples (>50 cm) to average out the inhomogeneity.

390

4.4 Gas-loss fractionation

In the outer ice, the $\delta\text{O}_2/\text{N}_2$ and $\delta\text{Ar}/\text{N}_2$ are significantly depleted and $\delta^{18}\text{O}$ is enriched due to post-coring gas loss, with higher storage temperature leading to larger fractionation (Fig. B4). The slope of $\Delta\delta\text{Ar}/\text{N}_2$ vs. $\Delta\delta\text{O}_2/\text{N}_2$ is 0.22 (Fig. 9f, Table C2), which is significantly smaller than those from the pairs of inner ice, suggesting that the process for gas loss is different from natural fractionation processes within the ice sheet. The slope of $\Delta\delta^{18}\text{O}$ vs. $\Delta\delta\text{O}_2/\text{N}_2$ is -0.0083 (Fig. B5), which is similar to those previously reported for artifactual gas loss from the Siple Dome (Severinghaus et al., 2009), WAIS Divide (Seltzer et al., 2017) and EDC (Extier et al., 2018) ice cores.

Severinghaus et al. (2009) extensively measured the Siple Dome ice core and found a tight relationship between $\Delta\delta\text{Ar}/\text{N}_2$ and $\Delta\delta\text{O}_2/\text{N}_2$ with the slope of ~ 0.5 , which was also typical for other ice cores that experienced large gas loss (Sowers et al., 1989; Bender et al., 1995). The slope of ~ 0.5 may be the combination of size-dependent fractionation (e.g., 1:1 for $\delta\text{O}_2/\text{N}_2$ and $\delta\text{Ar}/\text{N}_2$) and mass-dependent fractionation (1:3 for $\delta\text{O}_2/\text{N}_2$ and $\delta\text{Ar}/\text{N}_2$) (Severinghaus et al., 2009). The slope for the DF gas-loss fractionation (~ 0.2) is significantly smaller than most of the previous values, implying that mass-dependent fractionation may be more important for the storage condition of the DF core. Significant mass-dependent fractionation is expected for gas loss through micro-cracks (Bender et al., 1995). Thus, there may have been micro-cracks in the outer ice, although we did not observe visible cracks. The insensitivity of $\delta^{15}\text{N}$ to gas loss, consistent with earlier findings, may be explained by viscous flow for N_2 , or molecular-size-limited diffusion through ice matrix (Severinghaus et al., 2009).

405



5 Conclusions

410 The variations of $\delta\text{O}_2/\text{N}_2$ and $\delta\text{Ar}/\text{N}_2$ within the ice sheet from bubbly ice to clathrate hydrate ice at Dome Fuji are reconstructed
without post-coring gas-loss signals. Their variations in the bubbly ice zone, upper BCTZ and below BCTZ show close
similarity to the local summer insolation. Our $\delta\text{O}_2/\text{N}_2$ data from the clathrate hydrate ice zone agree with the previous data
after the gas-loss correction (Kawamura et al., 2007), with much less scatters, demonstrating that the original air composition
is preserved in the ice core stored at $-50\text{ }^\circ\text{C}$ and may be measured with our technique for precise orbital tuning. In the future,
415 the high-precision $\delta\text{O}_2/\text{N}_2$ and $\delta\text{Ar}/\text{N}_2$ data may also provide non-insolation signals on the gases and eventually be useful for
the reconstructions of past atmospheric oxygen and argon concentrations.

The large scatters in the lower BCTZ may be created by mm-scale vertical inhomogeneity of air composition combined with
finite sample length. The insolation signal originally recorded at the bubble close-off remains through the BCTZ, and the
insolation signal may be reconstructed by analyzing long ice samples ($>50\text{ cm}$).

420 Below the BCTZ, the scatters around the orbital-scale variability decrease with depth. The high-resolution analyses of five 50-
cm segments show decreasing cm-scale variability of $\delta\text{O}_2/\text{N}_2$ and $\delta\text{Ar}/\text{N}_2$ with depth, suggesting diffusive smoothing. A one-
dimensional gas diffusion model reproduces the smoothing in this zone with the permeation coefficients of Salamatin et al.
(2001).

425 The slope of the pair differences of $\delta\text{Ar}/\text{N}_2$ to $\delta\text{O}_2/\text{N}_2$ is about 1 in the BCTZ, and no correlation is found between those of
 $\delta^{18}\text{O}$ and $\delta\text{O}_2/\text{N}_2$, suggesting that the O_2 and Ar fractionations associated with the bubble-clathrate transition are mass-
independent. On the other hand, the slope for the bubble close-off process is around 0.5, suggesting a combination of mass-
independent and mass-dependent fractionation for O_2 and Ar. For the BCTZ, the slower molecular diffusion of Ar than O_2
430 may be canceled by the lower dissociation pressure of Ar than O_2 , which should produce a steeper Ar partial pressure gradient
from the bubbles to the growing clathrate. For the bubble close-off of small molecules, such a cancellation cannot occur, and
both the bond-breaking mechanism and the interstitial mechanism may play roles for the molecular diffusion through the thin
ice wall of fresh bubbles. The slope is small (0.2) in ice that experienced large gas loss, suggesting that mass-dependent
fractionation may be important for the storage condition of the DF core.

435



Appendix A: Diffusion model

A1 Model construction

We simulate diffusive smoothing of $\delta O_2/N_2$ and $\delta Ar/N_2$ in the clathrate hydrate ice zone with a simple one-dimensional gas diffusion model (Ikeda-Fukazawa et al., 2005; Bereiter et al., 2009; Bereiter et al., 2014). The model assumes that the molecular
 440 diffusion through the ice lattice is driven by the concentration gradient of dissolved gas in the ice, which is in equilibrium with clathrate hydrates. The governing equation is (see Table A1 for a full list of symbol meanings)

$$\frac{\partial c_m^h}{\partial t} = \frac{\partial}{\partial z} \left(D_m \frac{\partial c_m^h}{\partial z} \right), \quad (A1)$$

where D_m is the diffusivity of m -molecule in ice at 1 MPa and C_m^h is the concentration of m -molecule ($m = N_2, O_2$ or Ar) dissolved in ice in equilibrium with clathrate hydrate. C_m^h is expressed as

$$445 \quad C_m^h = S_m P_m^d X_m, \quad (A2)$$

where S_m is the solubility of m -molecule in ice at 1 MPa, X_m is the mean molar fraction of m -molecule in the clathrate hydrates, and P_m^d is the dissociation pressure of the m -molecule. The dissociation pressure (MPa) of m -molecule at temperature T (K) is given by (Miller, 1969; Kuhs et al., 2000) (Fig. A1)

$$\log P_m^d = a_m - \frac{b_m}{T}, \quad (A3)$$

450 where a_m and b_m are constant and shown in Table 2. Because there are no published values for a_{Ar} and b_{Ar} , we found them by fitting the dissociation pressures of argon hydrate vs. temperature measured by Nagashima et al. (2018) with eq. (A3) (Fig. A1). The a_{Ar} and b_{Ar} are 3.63 and 739.5, respectively. The molar fraction of the m -molecule in the clathrate hydrate is given by

$$X_m = \frac{U_m}{U_{N_2} + U_{O_2} + U_{Ar} + U_{others}^0}, \quad (A4)$$

455 where U_m is the concentration of m -molecule in total air content. U_{others}^0 is the concentration of minor gases, which is assumed to be constant and given by

$$U_{others}^0 = U^0 - U_{N_2}^0 - U_{O_2}^0 - U_{Ar}^0 = \frac{TAC \cdot M_{H_2O}}{V_{STP}} (1 - R_{N_2} - R_{O_2} - R_{Ar}), \quad (A5)$$

where U^0 is concentration of total air content in ice, U_m^0 is concentration of m -molecule with the atmospheric ratio in the total air content, TAC is total air content, M_{H_2O} is molar mass of ice (H_2O), V_{STP} is molar volume of a gas at standard temperature
 460 and pressure, and R_m is the atmospheric ratio of m -molecule.

The model uses an initial box height (Δz) of 5×10^{-3} m. The downward diffusive flux (f_m) of m -molecule per unit area at the top boundary of i -th box is the product of the diffusivity and concentration gradient:

$$f_{m(i)} = D_m \frac{c_{m(i-1)}^h - c_{m(i)}^h}{\Delta z \tau_r}. \quad (A6)$$



465 τ_r is relative thinning function (thinning function divided by that at the top of the model domain). By substituting eq. A2 into eq. A6, f_m is expressed as

$$f_{m(i)} = \frac{D_m S_m P_m^d}{\Delta z \tau_r} (X_{m(i-1)} - X_{m(i)}). \quad (\text{A7})$$

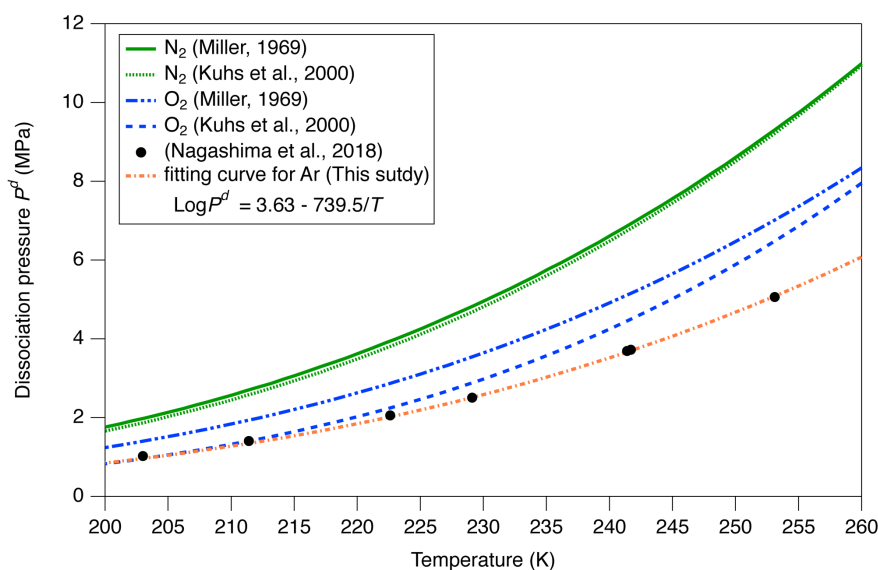
The net flux of m -molecule is

$$F_{m(i)} = \frac{f_{m(i)} - f_{m(i+1)}}{\Delta z \tau_r}, \quad (\text{A8})$$

470 and the concentration change of m -molecule in total air content becomes

$$\Delta U_{m(i)} = F_{m(i)} \Delta t, \quad (\text{A9})$$

where Δt is time step (~ 11.6 days).



475

Figure A1: Relationship between temperature and dissociation pressure for N_2 , O_2 (Miller, 1969; Kuhs et al., 2000) and Ar hydrates (Nagashima et al., 2018). The data for Ar hydrate (solid circles) is fitted with an exponential function: $\log P^d = 3.63 - 739.5/T$.

480

A2 Model input

The diffusivity D_m , solubility S_m , or their product (permeability, k_m) for air molecules are taken from the literature (Ikeda-Fukazawa et al., 2001; Salamatin et al., 2001; Ikeda-Fukazawa et al., 2005). Ikeda-Fukazawa et al. (2001) and Salamatin et al. (2001) estimated permeability of N_2 and O_2 , which were constrained by observed $\delta O_2/N_2$ of individual air inclusions in BCTZ.

485 Ikeda-Fukazawa et al. (2005) estimated solubility and diffusivity of N_2 and O_2 based on molecular dynamics simulations, and



the results were consistent with gas-loss fractionation for the Dome Fuji core. The permeability ($\text{m}^2 \text{s}^{-1}$) at T (K) and 1 MPa of Ikeda-Fukazawa et al. (2001) (hereafter IkFk01) is given by

$$k_m = k_m^0 P_m^d \exp\left(-\frac{E_m^k}{RT}\right), \quad (\text{A10})$$

where k_m^0 is a constant, E_m^k is activation energy of permeation for m -molecule, R is the gas constant. The permeability ($\text{m}^2 \text{s}^{-1}$) at temperature T (K) and 1MPa of Salamatin et al. (2001) (hereafter Salm01) is given by

$$k_m = k_m^0 \frac{P_m^d}{P_m^{220}} \exp\left[\frac{E_m^k}{R} \left(\frac{1}{220} - \frac{1}{T}\right)\right], \quad (\text{A11})$$

where P_m^{220} is dissociation pressure of m -molecule at 220 K. The diffusivity D_m or permeability k_m ($\text{m}^2 \text{s}^{-1}$) at temperature T (K) of Ikeda-Fukazawa et al. (2005) (hereafter IkFk05) is given by

$$D_m = D_m^0 \exp\left(-\frac{E_m^D}{RT}\right). \quad (\text{A12})$$

The solubility at 1MPa of Ikeda-Fukazawa et al. (2005) is given by

$$S_m = S_m^0 \exp\left(-\frac{E_m^S}{RT}\right), \quad (\text{A13})$$

where S_m^0 is a constant for m -molecule, E_m^S is activation energy of solubility for m -molecule. We used those permeation parameters for our model (parameters are summarized in Table A2 and each permeability is shown in Fig. 2 and Table A3).

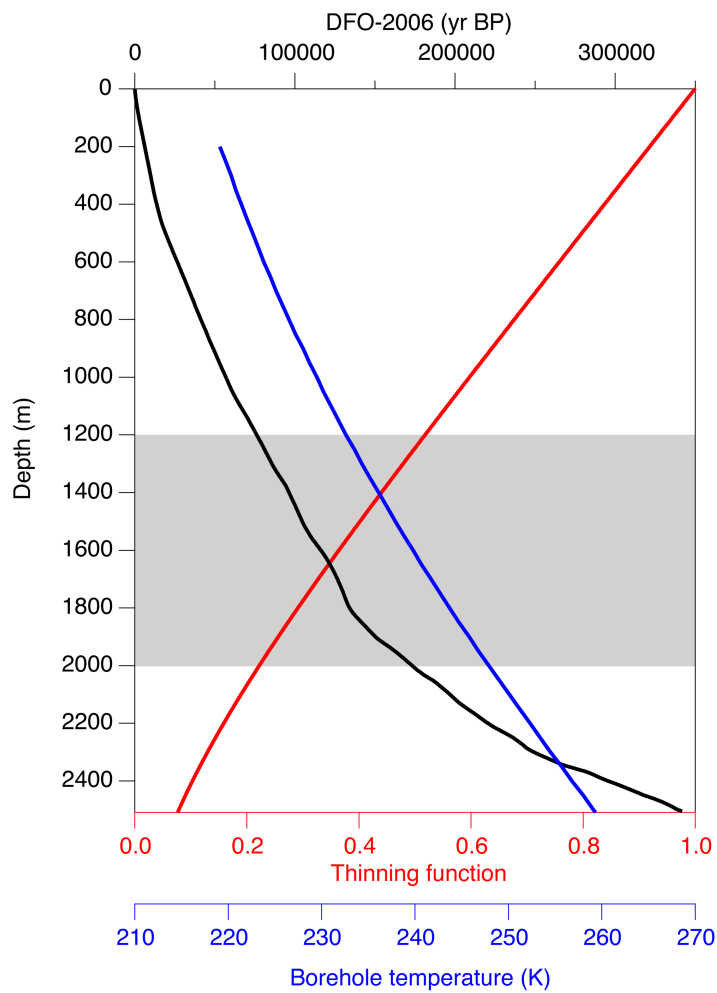
There are no published values of k_{Ar} , thus we estimated it from k_{N_2} and k_{O_2} in Salamatin et al. (2001) with two formulations by Kobashi et al. (2015). The first one $k_{Ar(I)}$ uses diffusion coefficients of N_2 , O_2 and Ar at 270 K from the molecular dynamic simulations by Ikeda-Fukazawa et al. (2004) ($D_{N_2}^{270}$: $2.1 \times 10^{-11} \text{ m}^2 \text{ s}^{-1}$, $D_{O_2}^{270}$: $4.7 \times 10^{-11} \text{ m}^2 \text{ s}^{-1}$ and D_{Ar}^{270} : $4.0 \times 10^{-11} \text{ m}^2 \text{ s}^{-1}$):

$$k_{Ar(I)} = k_{O_2} - \left(\frac{D_{O_2}^{270} - D_{Ar}^{270}}{D_{O_2}^{270} - D_{N_2}^{270}}\right) (k_{O_2} - k_{N_2}) \quad (\text{A14})$$

The second permeability $k_{Ar(II)}$ is based on the observations that $\delta Ar/N_2$ is often depleted about half of $\delta O_2/N_2$ (e.g., Severinghaus et al., 2009). The permeability of Ar(II) is expressed as

$$k_{Ar(II)} = \frac{(k_{N_2} + k_{O_2})}{2}. \quad (\text{A15})$$

Initial values of $\delta O_2/N_2$ and $\delta Ar/N_2$ are made by repeating the 2.5-cm continuous data at 1258 m (81.7 kyr BP) (Fig. 6), and initial total air content is constant over the model domain. Borehole temperature profile (T) (Buizert et al., 2021) and thinning function (Nakano et al., 2016) were used to simulate the evolution of layer thickness and temperature of the model domain (Fig. A2). We run the model for 100 kyr to cover the depth range covered by our data (until about 2000 m).



515

Figure A2: Thinning function (red, Nakano et al., 2016), temperature (blue, Buizert et al., 2021) and age (black, Kawamura et al., 2007) in the ice sheet at Dome Fuji used for the diffusion model. Grey shading indicates the depth range of the model run.



Table A1: List of symbols

Symbol	meaning	Unit
m	molecule species ($m = \text{N}_2, \text{O}_2$ or Ar)	
C_m^h	concentration of m -molecule	$\text{mol mol}_{\text{ice}}^{-1}$
P_m^d	dissociation pressure of m -molecule	MPa
X_m	molar fraction of m -molecule in the clathrate hydrate	
a_m	constant of dissociation pressure for m -molecule	
b_m	constant of dissociation pressure for m -molecule	K
T	temperature	K
U_m	concentration of m -molecule in total air content	$\text{mol mol}_{\text{ice}}^{-1}$
U^0	concentration of total air content in ice	$\text{mol mol}_{\text{ice}}^{-1}$
U_m^0	concentration of m -molecule with the atmospheric ratio in the total air content	$\text{mol mol}_{\text{ice}}^{-1}$
U_{others}^0	concentration of minor gases	$\text{mol mol}_{\text{ice}}^{-1}$
TAC	total air content	$\text{m}^3 \text{g}^{-1}$
$M_{\text{H}_2\text{O}}$	molar mass of ice (H_2O) (18.05128)	g mol^{-1}
V_{STP}	molar volume of a gas at 273.15K and 100 kPa (0.022711)	$\text{m}^3 \text{mol}^{-1}$
R_m	atmospheric ratio of m -molecule	
k_m	permeation coefficient of m -molecule in ice	$\text{m}^2 \text{s}^{-1}$
k_m^0	constant of permeation for m -molecule in ice,	$\text{m}^2 \text{s}^{-1}$
D_m	diffusion coefficient of m -molecule in ice	$\text{m}^2 \text{s}^{-1}$
D_m^0	constant of diffusion for m -molecule in ice,	$\text{m}^2 \text{s}^{-1}$
S_m	solubility of m -molecule in ice	$\text{mol mol}_{\text{ice}}^{-1} \text{MPa}^{-1}$
S_m^0	constant of solution for m -molecule in ice	$\text{mol mol}_{\text{ice}}^{-1} \text{MPa}^{-1}$
E_m^k	activation energy of permeation for m -molecule in ice	kJ mol^{-1}
E_m^D	activation energy of diffusion for m -molecule in ice	kJ mol^{-1}
E_m^S	activation energy of solubility for m -molecule in ice	kJ mol^{-1}
R	gas constant (8.314)	$\text{kJ mol}^{-1} \text{K}^{-1}$
f_m	diffusive flux of m -molecule	$\text{mol m}^{-2} \text{s}^{-1}$
F_m	net flux of m -molecule dissolved in ice	mol s^{-1}
Δz	grid size	m
τ_r	relative thinning function	
Δt	time step	s



520 **Table A2:** Model parameters

		IkFk01	Salm01	IkFk05
constant of dissociation pressure for N ₂	a_{N_2}	3.6905 ^a	3.6905 ^a	3.77 ^b
constant of dissociation pressure for O ₂	b_{N_2}	688.9 ^a	688.9 ^a	4.17 ^b
constant of dissociation pressure for N ₂ (K)	a_{O_2}	3.679 ^a	3.67 ^a	710 ^b
constant of dissociation pressure for O ₂ (K)	b_{O_2}	717 ^a	717 ^a	850 ^b
constant of diffusion or permeation for N ₂ in ice (m ² s ⁻¹)	$k_{N_2}^0$	2.4×10 ^{-9c}	5.7×10 ^{-22d}	-
constant of diffusion or permeation for O ₂ in ice (m ² s ⁻¹)	$k_{O_2}^0$	2.4×10 ^{-8c}	1.7×10 ^{-21d}	-
constant of solution for N ₂ in ice (mol mol _{ice} ⁻¹ MPa ⁻¹)	$S_{N_2}^0$	-	-	4.5×10 ^{-7e}
constant of solution for O ₂ in ice (mol mol _{ice} ⁻¹ MPa ⁻¹)	$S_{O_2}^0$	-	-	3.7×10 ^{-7e}
constant of diffusion for N ₂ in ice (m ² s ⁻¹)	$D_{N_2}^0$	-	-	2.0×10 ^{-10e}
constant of diffusion for O ₂ in ice (m ² s ⁻¹)	$D_{O_2}^0$	-	-	3.5×10 ^{-9e}
activation energy of permeation for N ₂ in ice (kJ mol ⁻¹)	$E_{N_2}^k$	55.57 ^c	50 ^d	-
activation energy of permeation for O ₂ in ice (kJ mol ⁻¹)	$E_{O_2}^k$	55.57 ^c	50 ^d	-
activation energy of solution for N ₂ in ice (kJ mol ⁻¹)	$E_{N_2}^s$	-	-	9.2 ^e
activation energy of solution for O ₂ in ice (kJ mol ⁻¹)	$E_{O_2}^s$	-	-	7.9 ^e
activation energy of diffusion for N ₂ in ice (kJ mol ⁻¹)	$E_{N_2}^d$	-	-	5.1 ^e
activation energy of diffusion for O ₂ in ice (kJ mol ⁻¹)	$E_{O_2}^d$	-	-	9.7 ^e

^a Miller (1969), ^b Kuhs et al. (2000), ^c Ikeda-Fukazawa et al. (2001), ^d Salamatin et al. (2001), ^e Ikeda-Fukazawa et al. (2005).

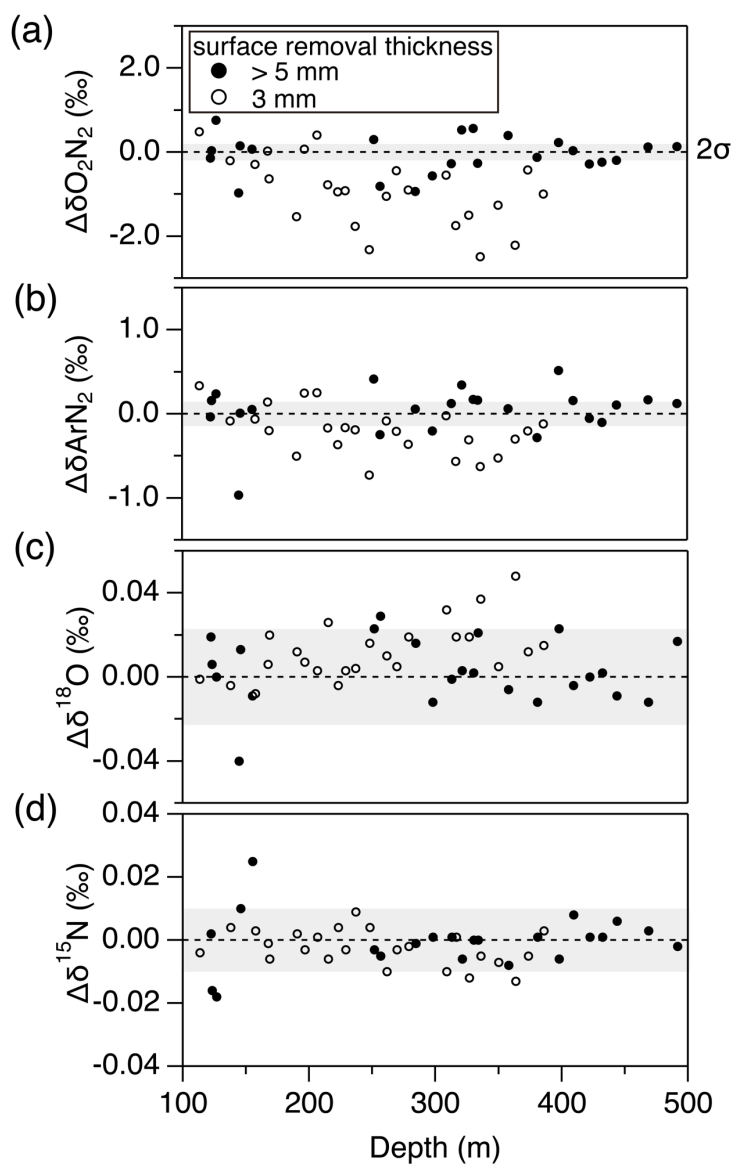
Table A3: Examples of dissociation pressure, diffusivity, solubility and permeability (at 240 K)

		IkFk01	Salm01	IkFk05	Ar (I)	Ar (II)
Dissociation pressure of N ₂ (MPa)	$p_{N_2}^d$	6.48 ^a	6.61 ^b	6.48 ^a		
Dissociation pressure of O ₂ (MPa)	$p_{O_2}^d$	4.25 ^a	4.92 ^b	4.25 ^a		
Dissociation pressure of Ar (MPa)	p_{Ar}^d				3.54	3.54
Diffusivity of N ₂ (m ² s ⁻¹)	D_{N_2}			1.55×10 ⁻¹¹		
Diffusivity of O ₂ (m ² s ⁻¹)	D_{O_2}			2.71×10 ⁻¹¹		
Solubility of N ₂ (mol mol _{ice} ⁻¹ MPa ⁻¹)	S_{N_2}			4.48×10 ⁻⁹		
Solubility of O ₂ (mol mol _{ice} ⁻¹ MPa ⁻¹)	S_{O_2}			7.06×10 ⁻⁹		
Permeability of N ₂ (m ² s ⁻¹ MPa ⁻¹)	k_{N_2}	1.27×10 ⁻²⁰	1.02×10 ⁻²⁰	6.95×10 ⁻²⁰		
Permeability of O ₂ (m ² s ⁻¹ MPa ⁻¹)	k_{O_2}	9.49×10 ⁻²⁰	3.12×10 ⁻²⁰	1.91×10 ⁻¹⁹		
Permeability of Ar (m ² s ⁻¹ MPa ⁻¹)	k_{Ar}				2.55×10 ⁻²⁰	2.07×10 ⁻²⁰

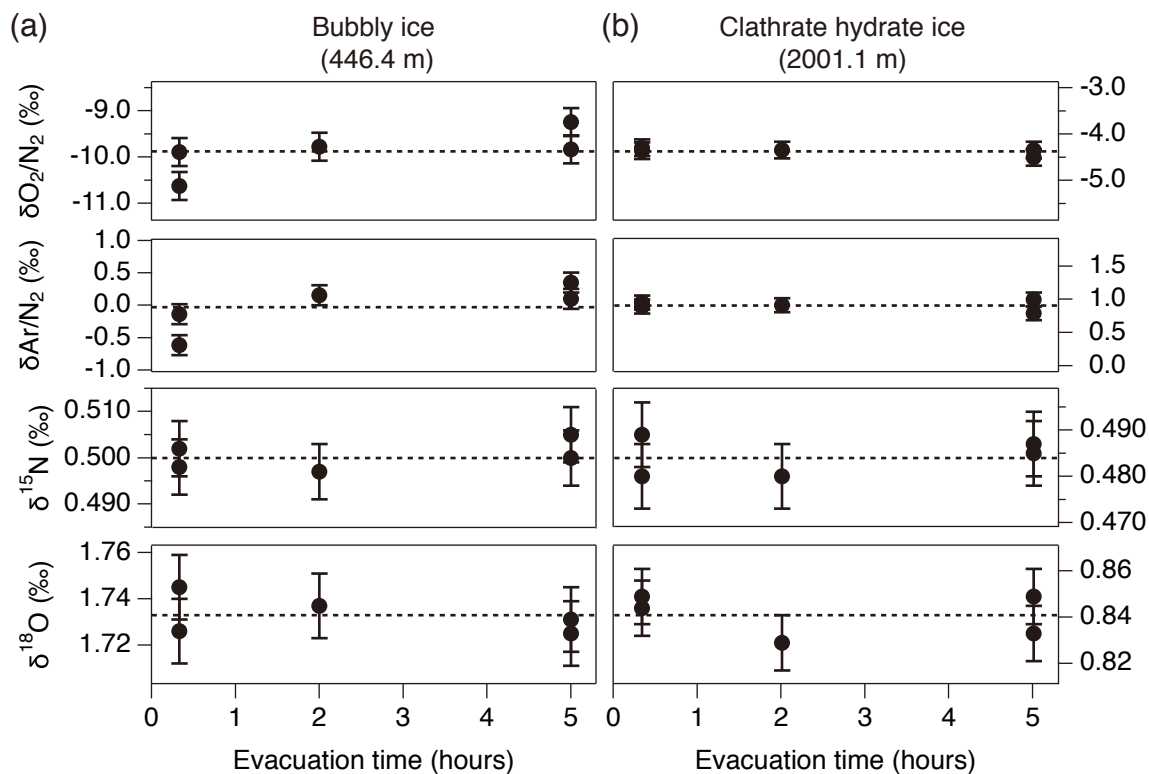
^a Miller (1969), ^b Kuhs et al. (2000).



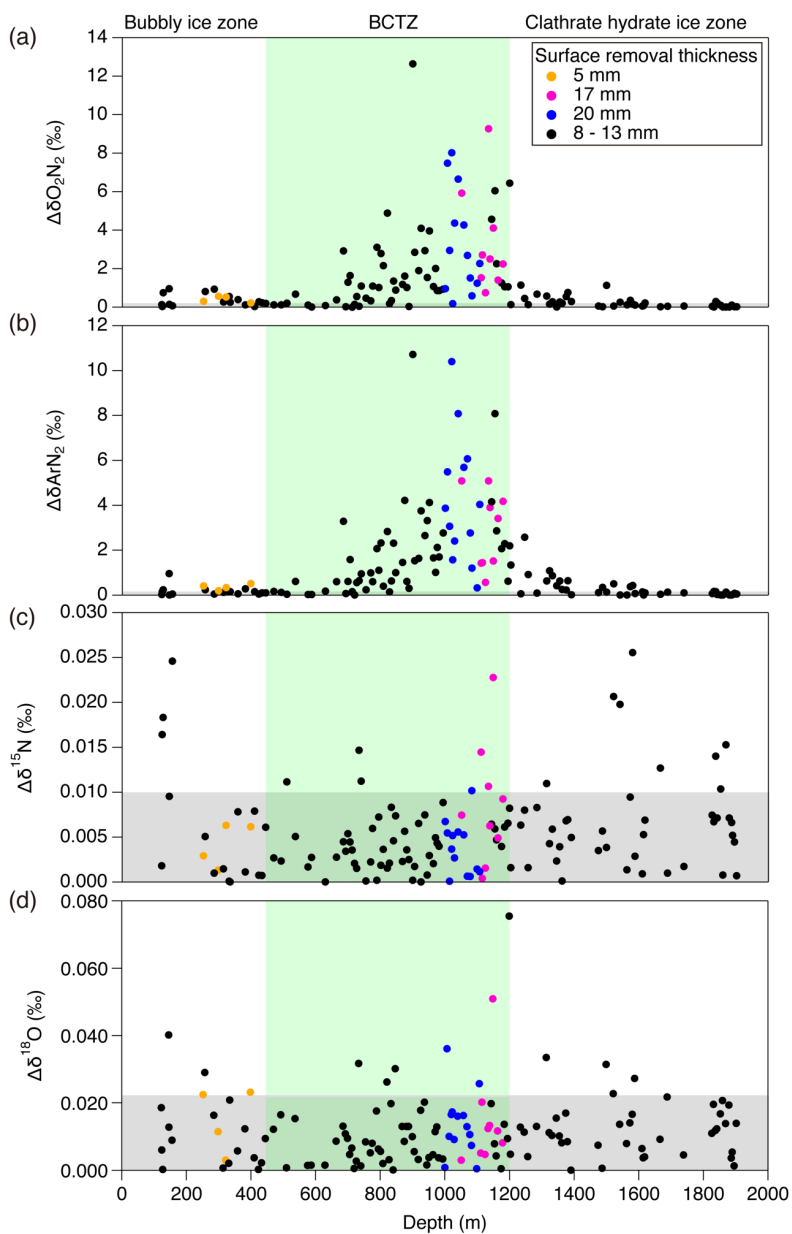
525 Appendix B: Supplementary figures



530 **Figure B1:** Pair difference (“a2” piece minus “a1” piece, Fig. 1) in the bubbly ice for (a) $\delta\text{O}_2/\text{N}_2$, (b) $\delta\text{Ar}/\text{N}_2$ (c) $\delta^{18}\text{O}$ and (d) $\delta^{15}\text{N}$. Solid circles are the data from the samples after removing the outer ice by > 5-mm thickness, and open circles are the data with ~3-mm removal. Grey shadings are 2 pooled standard deviations of the pair differences for clathrate ice, shown as uncertainty estimates.



535 **Figure B2:** Results of the evacuation experiment for $\delta\text{O}_2/\text{N}_2$, $\delta\text{Ar}/\text{N}_2$, $\delta^{15}\text{N}$ and $\delta^{18}\text{O}$ in (a) bubbly ice (446.4 m) and (b) clathrate hydrate ice (2001.1 m). Dashed lines are the average of all 5 values.



540 **Figure B3:** Absolute pair differences of (a) $\delta\text{O}_2/\text{N}_2$, (b) $\delta\text{Ar}/\text{N}_2$, (c) $\delta^{15}\text{N}$ and (d) $\delta^{18}\text{O}$. Grey shadings indicate the 2 pooled standard deviations for clathrate hydrate ice.

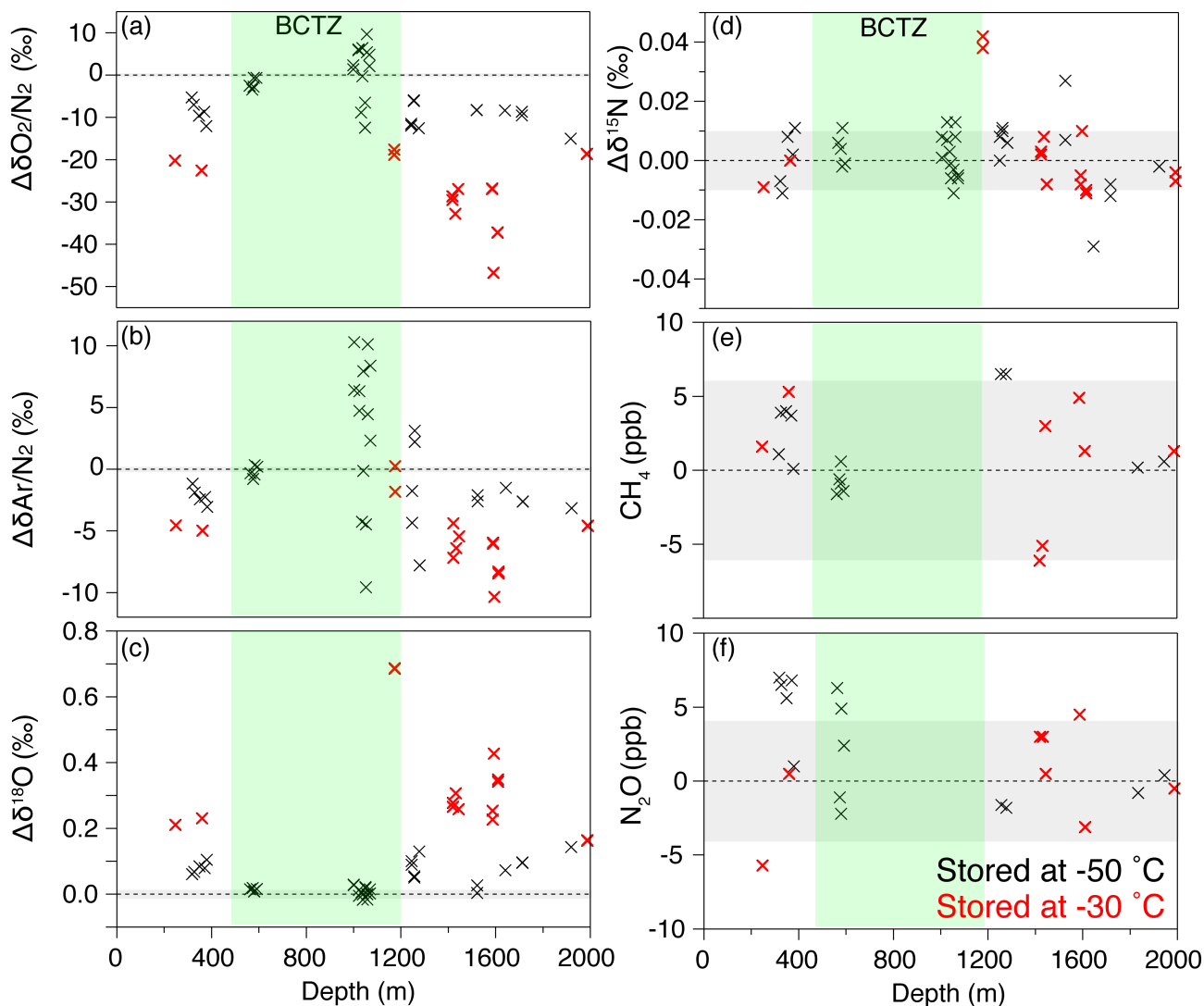
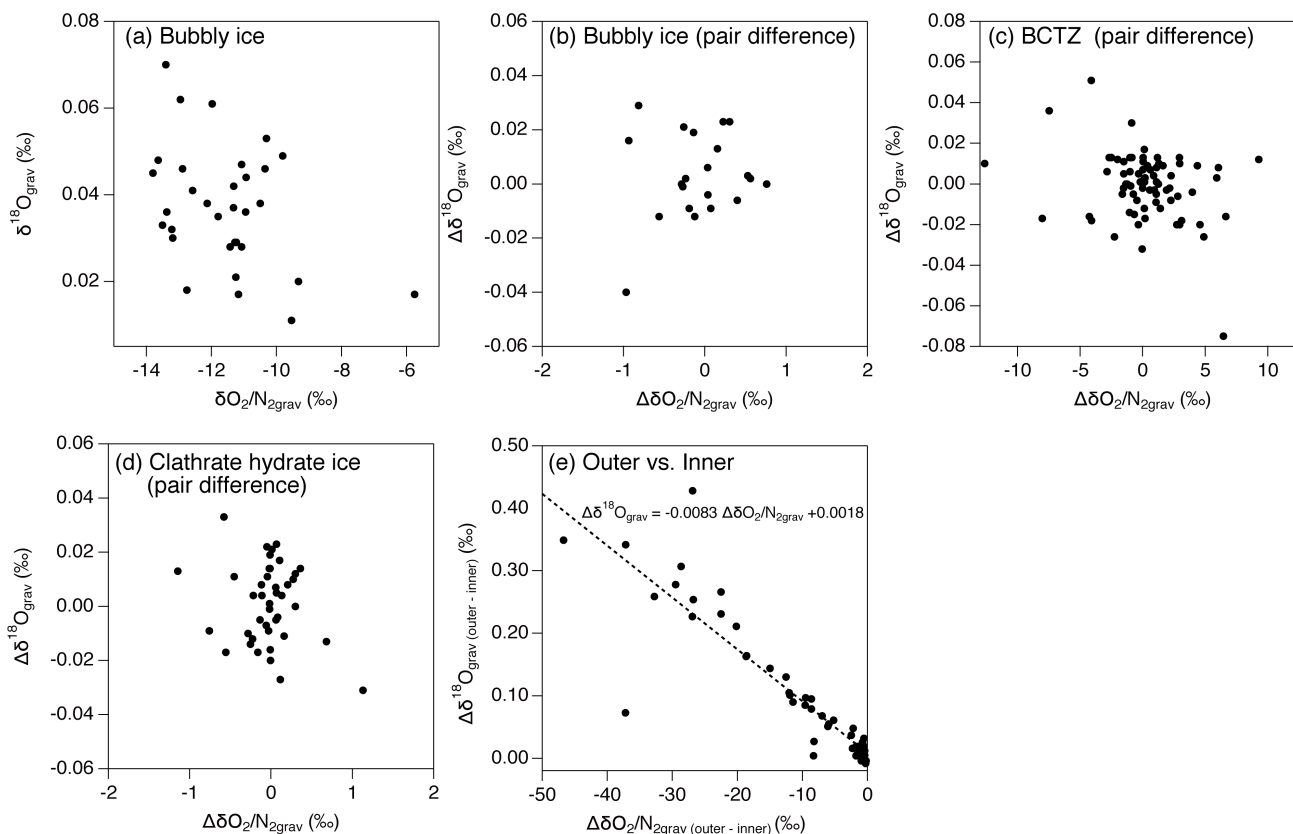


Figure B4: Differences of the values in the outer and inner pieces (outer minus inner) for (a) $\delta\text{O}_2/\text{N}_2$, (b) $\delta\text{Ar}/\text{N}_2$, (c) $\delta^{18}\text{O}$, (d) $\delta^{15}\text{N}$, (e) CH_4 concentration, and (f) N_2O concentration. Grey shadings indicate 2σ pooled standard deviations of pair differences (from inner ice only) in the clathrate hydrate ice. Black and red markers are the data using the outer samples stored at $-50\text{ }^\circ\text{C}$ and $-30\text{ }^\circ\text{C}$, respectively.



545

Figure B5: Relationship between $\delta\text{O}_2/\text{N}_2$ and $\delta^{18}\text{O}$ for (a) the last 2000 years for bubbly ice, (b) pair differences in bubbly ice zone, (c) pair differences in BCTZ, (d) pair differences in clathrate hydrate ice zone, and (e) differences between the outer ice and inner ice (bubbly ice and clathrate hydrate ice).



Appendix C: Supplementary tables

550 **Table C1:** Pooled standard deviations for $\delta^{15}\text{N}$, $\delta\text{O}_2/\text{N}_2_{\text{grav corr.}}$ and $\delta\text{Ar}/\text{N}_2_{\text{grav corr.}}$ (‰).

	$\delta^{15}\text{N}$	$\delta\text{O}_2/\text{N}_2_{\text{grav corr.}}$	$\delta\text{Ar}/\text{N}_2_{\text{grav corr.}}$	n
112 – 450 m (bubbly ice)	0.006	0.305	0.154	20
450 – 800 m (upper BCTZ)	0.004	0.862	0.776	24
800 – 1200 m (lower BCTZ)	0.005	2.662	2.555	46
1200 – 1480 m (clathrate hydrate ice)	0.004	0.599	0.565	13
1480 – 1980 m (clathrate hydrate ice)	0.007	0.184	0.112	26

Table C2: Slopes for $\delta\text{Ar}/\text{N}_2$ vs. $\delta\text{O}_2/\text{N}_2$ and for $\Delta\delta\text{Ar}/\text{N}_2$ vs. $\Delta\delta\text{O}_2/\text{N}_2$.

	Site name	Zone	Remarks	Slope	1 σ	Reference for the original data
$\delta\text{Ar}/\text{N}_2/\delta\text{O}_2/\text{N}_2$	Dome Fuji	All (112 – 1980 m)	well preserved	0.51	0.01	This study
	Dome Fuji	Bubbly ice (112 – 450m)	well preserved	0.50	0.01	This study
	Dome Fuji	Upper BCTZ (450 – 800 m)	well preserved	0.45	0.01	This study
	Dome Fuji	Lower BCTZ (800 – 1200 m)	well preserved	0.61	0.01	This study
	Dome Fuji	Clathrate hydrate (1200 – 1980 m)	well preserved	0.42	0.02	This study
	Dome Fuji	Outer ice	significantly affected by gas loss	0.25	0.01	This study
	9 sites ^a	Bubbly ice		0.46	0.03	Sowers et al. (1989)
	Byrd	All (145 – 2100 m)	extremely negative below 1800 m	0.42	0.01	Bender et al. (1995)
	Vostok-3G	All (140 – 2058 m)	thermally drilled	0.70	0.01	Bender et al. (1995)
	Dome C	Bubbly ice (180 – 625 m)	poor quality	0.26	0.01	Bender et al. (1995)
	GISP2	Bubbly ice (73 – 213 m)		0.54	0.03	Bender et al. (1995)
	Siple Dome	Bubbly ice (75 – 973 m)	highly fractured	0.58	0.01	Severinghaus et al. (2009)
	WAIS Divide	All (80 – 2625 m)	slightly affected by gas loss	0.93	0.01	Seltzer et al. (2017)
	WAIS Divide	Bubbly ice (80 – 2625 m)	slightly affected by gas loss	0.64	0.01	Seltzer et al. (2017)
	WAIS Divide	BCTZ (650 – 1600 m)	slightly affected by gas loss	1.00	0.01	Seltzer et al. (2017)
	WAIS Divide	Clathrate hydrate (1600 – 2625 m)	slightly affected by gas loss	0.97	0.01	Seltzer et al. (2017)
	SPICE	Bubbly ice (125 – 700 m)	slightly affected by gas loss	0.60	0.05	Severinghaus (2019)
	SPICE	BCTZ (700 – 1140 m)	slightly affected by gas loss	1.47	0.07	Severinghaus (2019)
	SPICE	Clathrate hydrate (1140 – m)	slightly affected by gas loss	0.54	0.01	Severinghaus (2019)
	NEEM	Bubbly ice (112 – 460 m)	slightly affected by gas loss	0.45	0.01	Oyabu et al. (2020)



	Dome Fuji	Bubbly ice (112 – 450m)	well preserved	0.53	0.08	This study
	Dome Fuji	Upper BCTZ (450 – 800 m)	well preserved	0.92	0.03	This study
	Dome Fuji	Lower BCTZ (800 – 1200 m)	well preserved	1.01	0.03	This study
	Dome Fuji	Clathrate hydrate (1200 – 1980 m)	well preserved	not detectable		This study
	Dome Fuji	Outer piece vs inner piece		0.22	0.01	This study
	Byrd	All (145 – 2100 m)	extremely negative below 1800 m	0.47	0.01	Bender et al. (1995)
	Vostok-3G	All (140 – 2058 m)	thermally drilled	0.54	0.03	Bender et al. (1995)
$\Delta\delta_{Ar}/N_2/\Delta\delta_{O_2}/N_2$ (pair difference)	Dome C	Bubbly ice (180 – 625 m)	poor quality	0.24	0.03	Bender et al. (1995)
	Siple Dome	Bubbly ice (75 – 973 m)	highly fractured	0.67	0.01	Severinghaus et al. (2009)
	WAIS Divide	Bubbly ice (80 – 650 m)	slightly affected by gas loss	0.72	0.01	Seltzer et al. (2017)
	WAIS Divide	BCTZ (650 – 1600 m)	slightly affected by gas loss	1.19	0.01	Seltzer et al. (2017)
	WAIS Divide	Clathrate hydrate (1600 – 3396 m)	slightly affected by gas loss	2.10	0.01	Seltzer et al. (2017)
	SPICE	Bubbly ice (- 700 m)	slightly affected by gas loss	0.84	0.06	Severinghaus (2019)
	SPICE	BCTZ (700 – 1140 m)	slightly affected by gas loss	0.88	0.06	Severinghaus (2019)
	SPICE	Clathrate hydrate (1140 – m)	slightly affected by gas loss	1.60	0.08	Severinghaus (2019)
	NEEM	Bubbly ice (112 – 460 m)	slightly affected by gas loss	0.62	0.01	Oyabu et al. (2020)

^a Byrd, Camp Century, Crete, Dominion Range, Dye 3, D10, D57 and Dome C ice cores.



555 **Data availability**

All data presented in this study is available at the NIPR ADS data repository (<https://ads.nipr.ac.jp/dataset/A20210430-001>) and will be available on the NOAA paleoclimate database.

Author contribution

IO: Conceptualization, Methodology, Validation, Formal analysis, Investigation, Data Curation, Writing - Original Draft,
560 Visualization, Funding acquisition. KeK: Conceptualization, Methodology, Validation, Investigation, Writing - Original Draft,
Supervision, Project administration, Funding acquisition. TU: Writing - Review & Editing. SF: Writing - Review & Editing.
KyK: Methodology, Validation, Investigation. MH: Validation, Investigation, SA: Methodology, Validation, Investigation.
SM: Methodology, Validation, Investigation. TN: Methodology, Validation, Investigation. JS: Investigation, Writing - Review
& Editing, JM: Formal analysis, Investigation, Writing - Review & Editing.

565 **Competing interests**

The authors declare that they have no conflict of interest.

Acknowledgments

We are grateful to Hiroshi Ohno of Kitami Institute of Technology for providing air inclusion data and comments, Tomoko
Fukazawa of Meiji University for providing the Raman O₂/N₂ data, Kumiko Goto-Azuma of National Institute of Polar
570 Research for the management of ice-core chemistry analyses, Hirohisa Matsushima, Satoko Nakanishi, Mariko Hayakawa,
Akito Tanaka, Satomi Oda, Maki Nakatani, Yasuko Fukagawa, Miho Arai and Ryo Inoue for ice core measurements. We
acknowledge the Dome Fuji ice core projects, the Japanese Antarctic Research Expedition, and Ice Core Consortium. This
study was supported by Japan Society for the Promotion of Science (JSPS) and Ministry of Education, Culture, Sports, Science
and Technology-Japan (MEXT) KAKENHI Grant Numbers 20H04327, 17K12816 and 17J00769 to IO, 20H00639, 17H06320,
575 15KK0027 and 26241011 to KeK, 18H05294 to SF, and by NIPR Research Projects (Senshin Project and KP305).



Reference

- 580 Azuma, N., Wang, Y., Yoshida, Y., and Narita, H.: Crystallographic analysis of the Dome Fuji ice core, *Physics of Ice Core Records*, 45-61, <http://hdl.handle.net/2115/32461>, 2000.
- Battle, M., Bender, M., Sowers, T., Tans, P. P., Butler, J. H., Elkins, J. W., Ellis, J. T., Conway, T., Zhang, N., Lang, P., and Clarke, A. D.: Atmospheric gas concentrations over the past century measured in air from firn at the South Pole, *Nature*, 383, 231-235, <https://doi.org/10.1038/383231a0>, 1996.
- 585 Battle, M. O., Severinghaus, J. P., Sofen, E. D., Plotkin, D., Orsi, A. J., Aydin, M., Montzka, S. A., Sowers, T., and Tans, P. P.: Controls on the movement and composition of firn air at the West Antarctic Ice Sheet Divide, *Atmos. Chem. Phys.*, 11, 11007-11021, <https://doi.org/10.5194/acp-11-11007-2011>, 2011.
- Bazin, L., Landais, A., Capron, E., Masson-Delmotte, V., Ritz, C., Picard, G., Jouzel, J., Dumont, M., Leuenberger, M., and Prié, F.: Phase relationships between orbital forcing and the composition of air trapped in Antarctic ice cores, *Clim. Past*, 12, 729-748, <https://doi.org/10.5194/cp-12-729-2016>, 2016.
- 590 Bender, M., Sowers, T., and Lipenkov, V.: On the concentrations of O₂, N₂, and Ar in trapped gases from ice cores, *J. Geophys. Res.*, 100, 18651-18660, <https://doi.org/10.1029/94JD02212>, 1995.
- Bender, M., Sowers, T., Barnola, J.-M., and Chappellaz, J.: Changes in the O₂/N₂ ratio of the atmosphere during recent decades reflected in the composition of air in the firn at Vostok Station, Antarctica, *J. Geophys. Res.*, 21, 189-192, <https://doi.org/10.1029/93GL03548>, 1994a.
- Bender, M. L.: Orbital tuning chronology for the Vostok climate record supported by trapped gas composition, *Earth Planet. Sci. Lett.*, 204, 275-289, [https://doi.org/10.1016/S0012-821X\(02\)00980-9](https://doi.org/10.1016/S0012-821X(02)00980-9), 2002.
- Bender, M. L., Tans, P. P., Ellis, J. T., Orchardo, J., and Habfast, K.: A high precision isotope ratio mass spectrometry method for measuring the O₂/N₂ ratio of air, *Geochim. Cosmochim. Acta*, 58, 4751-4758, [https://doi.org/10.1016/0016-7037\(94\)90205-4](https://doi.org/10.1016/0016-7037(94)90205-4), 1994b.
- 600 Bereiter, B., Fischer, H., Schwander, J., and Stocker, T. F.: Diffusive equilibration of N₂, O₂ and CO₂ mixing ratios in a 1.5-million-years-old ice core, *The Cryosphere*, 8, 245-256, <https://doi.org/10.5194/tc-8-245-2014>, 2014.
- Bereiter, B., Schwander, J., Luthi, D., and Stocker, T. F.: Change in CO₂ concentration and O₂/N₂ ratio in ice cores due to molecular diffusion, *Geophys. Res. Lett.*, 36, L05703-05705, <https://doi.org/10.1029/2008GL036737>, 2009.
- 605 Buizert, C., Fudge, T. J., Roberts, W. H. G., Steig, E. J., Sherriff-Tadano, S., Ritz, C., Lefebvre, E., Edwards, J., Kawamura, K., Oyabu, I., Motoyama, H., Kahle, E. C., Jones, T. R., Abe-Ouchi, A., Obase, T., Martin, C., Corr, H., Severinghaus, J. P., Beaudette, R., Epifanio, J. A., Brook, E. J., Martin, K., Chappellaz, J., Aoki, S., Nakazawa, T., Sowers, T., Alley, R., Ahn, J., Sigl, M., Severi, M., Dunbar, N. W., Svensson, A., Fegyveresi, J., He, C., Liu, Z., Zhu, J., Otto-Bliesner, B., Lipenkov, V., Kageyama, M., and Schwander, J.: Antarctic-wide surface temperature and elevation during the Last Glacial Maximum, in press, 2021.
- 610



- Chazallon, B., Champagnon, B., Panczer, G., Pauer, F., Klapproth, A., and Kuhs, W. F.: Micro-Raman analysis of synthetic air clathrates, *European J. Mineral.*, 10, 1125-1134, 1998.
- Craig, H. and Scarsi, P.: Helium isotope stratigraphy in the GISP2 ice core, *Eos*, 78, 1997.
- Craig, H., Horibe, Y., and Sowers, T.: Gravitational separation of gases and isotopes in polar ice caps, *Science*, 23, 1675-1678, 615 <https://doi.org/10.1126/science.242.4886.1675>, 1988.
- Extier, T., Landais, A., Bréant, C., Prié, F., Bazin, L., Dreyfus, G., Roche, D. M., and Leuenberger, M.: On the use of $\delta^{18}\text{O}_{\text{atm}}$ for ice core dating, *Quat. Sci. Rev.*, 185, 244-257, <https://doi.org/10.1016/j.quascirev.2018.02.008>, 2018.
- Fujita, S., Okuyama, J., Hori, A., and Hondoh, T.: Metamorphism of stratified firn at Dome Fuji, Antarctica: A mechanism for local insolation modulation of gas transport conditions during bubble close off, *J. Geophys. Res.*, 114, 620 <https://doi.org/10.1029/2008JF001143>, 2009.
- Fujita, S., Goto-Azuma, K., Hirabayashi, M., Hori, A., Iizuka, Y., Motizuki, Y., Motoyama, H., and Takahashi, K.: Densification of layered firn in the ice sheet at Dome Fuji, Antarctica, *J. Glaciol.*, 62, 103-123, <https://doi.org/10.1017/jog.2016.16>, 2016.
- Goto-Azuma, K., Hirabayashi, M., Motoyama, H., Miyake, T., Kuramoto, T., Uemura, R., Igarashi, M., Iizuka, Y., Sakurai, 625 T., Horikawa, S., Suzuki, K., Suzuki, T., Fujita, K., Kondo, Y., Hattori, S., and Fujii, Y.: Reduced marine phytoplankton sulphur emissions in the Southern Ocean during the past seven glacials, *Nat. Commun*, 10, <https://doi.org/10.1038/s41467-019-11128-6>, 2019.
- Hondoh, T., Hondoh, T. (Ed.): An Overview of Microphysical Processes in Ice Sheets: Toward Nanoglaciology, Low Temperature Science, Physics of Ice Core Records II, Institute of Low Temperature Science, Hokkaido University, Japan, 630 <http://hdl.handle.net/2115/45404>, 2009.
- Hoshina, Y., Fujita, K., Nakazawa, F., Iizuka, Y., Miyake, T., Hirabayashi, M., Kuramoto, T., Fujita, S., and Motoyama, H.: Effect of accumulation rate on water stable isotopes of near-surface snow in inland Antarctica, *Journal of Geophysical Research: Atmospheres*, 119, 274-283, <https://doi.org/10.1002/2013JD020771>, 2014.
- Huber, C. and Leuenberger, M.: Measurements of isotope and elemental ratios of air from polar ice with a new on-line 635 extraction method, *Geochem. Geophys. Geosyst.*, 5, 1-13, <https://doi.org/10.1029/2004GC000766>, 2004.
- Huber, C., Beyerle, U., Leuenberger, M., Schwander, J., Kipfer, R., Spahni, R., Severinghaus, J. P., and Weiler, K.: Evidence for molecular size dependent gas fractionation in firn air derived from noble gases, oxygen, and nitrogen measurements, *Earth Planet. Sci. Lett.*, 243, 61-73, <https://doi.org/10.1016/j.epsl.2005.12.036>, 2006.
- Ikeda-Fukazawa, T., Kawamura, K., and Hondoh, T.: Diffusion of nitrogen gas in ice Ih, *Chemical Physics Letters*, 385, 467- 640 471, <https://doi.org/10.1016/j.cplett.2004.01.021>, 2004.
- Ikeda-Fukazawa, T., Hondoh, T., Fukumura, T., Fukazawa, H., and Mae, S.: Variation in N_2/O_2 ratio of occluded air in Dome Fuji antarctic ice, *J. Geophys. Res.*, 106, 17799-17810, <https://doi.org/10.1029/2000JD000104>, 2001.



- Ikeda-Fukazawa, T., Fukumizu, K., Kawamura, K., Aoki, S., Nakazawa, T., and Hondoh, T.: Effects of molecular diffusion on trapped gas composition in polar ice cores, *Earth Planet. Sci. Lett.*, 229, 183-192, 645 <https://doi.org/doi/10.1016/j.epsl.2004.11.011>, 2005.
- Kawamura, K., Parrenin, F., Lisiecki, L., Uemura, R., Vimeux, F., Severinghaus, J. P., Hutterli, M. A., Nakazawa, T., Aoki, S., Jouzel, J., Raymo, M. E., Matsumoto, K., Nakata, H., Motoyama, H., Fujita, S., Goto-Azuma, K., Fujii, Y., and Watanabe, O.: Northern Hemisphere forcing of climatic cycles in Antarctica over the past 360,000 years, *Nature*, 448, 912-916, <https://doi.org/10.1038/nature06015>, 2007.
- 650 Kobashi, T., Severinghaus, J. P., and Kawamura, K.: Argon and nitrogen isotopes of trapped air in the GISP2 ice core during the Holocene epoch (0–1,500 B.P.): Methodology and implications for gas loss processes, *Geochim. Cosmochim. Acta*, 72, 4675-4686, <https://doi.org/10.1016/j.gca.2008.07.006>, 2008.
- Kobashi, T., Ikeda-Fukazawa, T., Suwa, M., Schwander, J., Kameda, T., Lundin, J., Hori, A., Motoyama, H., Döring, M., and Leuenberger, M.: Post-bubble close-off fractionation of gases in polar firn and ice cores: effects of accumulation rate on 655 permeation through overloading pressure, *Atmos. Chem. Phys.*, 15, 13895-13914, <https://doi.org/10.5194/acp-15-13895-2015>, 2015.
- Kuhs, W. F., Klapproth, A., and Chazallon, B.: Chemical physics of air clathrate hydrates, in: T. Hondoh (Ed.), *Physics of Ice Cores Records*, Hokkaido University Press, Sapporo, 373-392, 2000.
- Lipenkov, V. Y.: Air bubbles and air-hydrate crystals in the Vostok ice core, *Physics of Ice Core Records*, 327-358, 2000.
- 660 Lüthi, D., Bereiter, B., Stauffer, B., Winkler, R., Schwander, J., Kindler, P., Leuenberger, M., Kipfstuhl, J., Capron, E., Landais, A., Fischer, H., and Stocker, T. F.: CO₂ and O₂/N₂ variations in and just below the bubble-clathrate transformation zone of Antarctic ice cores, *Earth Planet. Sci. Lett.*, 297, 226-233, <https://doi.org/10.1016/j.epsl.2010.06.023>, 2010.
- Miller, S. L.: Clathrate hydrates of air in Antarctic ice, *Science*, 165, 489-490, <https://doi.org/10.1126/science.165.3892.489>, 1969.
- 665 Nagashima, H. D., Nemoto, K., and Ohmura, R.: Phase equilibrium for argon clathrate hydrate at the temperatures from 197.6 K to 274.1 K, *J. Chem. Thermodynamics*, 127, 86-91, <https://doi.org/10.1016/j.jct.2018.07.019>, 2018.
- Nakano, S., Suzuki, K., Kawamura, K., Parrenin, F., and Higuchi, T.: A sequential Bayesian approach for the estimation of the age-depth relationship of the Dome Fuji ice core, *Nonlin. Process Geophys.*, 23, 31-44, <https://doi.org/10.5194/npg-23-31-2016>, 2016.
- 670 Narita, H., Azuma, N., Hondoh, T., Fujii, M., Kawaguchi, M., Mae, S. J., Shoji, H., Kameda, T., and Watanabe, O.: Characteristics of air bubbles and hydrates in the Dome Fuji ice core, Antarctica, *Ann. Glaciol.*, 29, 207-210, <https://doi.org/10.3189/172756499781821300>, 1999.
- Ohno, H., Iizuka, Y., and Fujita, S.: Pure rotational Raman spectroscopy applied to N₂/O₂ analysis of air bubbles in polar firn, *J. Glaciol.*, , 1-6, <https://doi.org/10.1017/jog.2021.40>, 2021.
- 675 Ohno, H., Lipenkov, V., and Hondoh, T.: Air bubble to clathrate hydrate transformation in polar ice sheets: A reconsideration based on the new data from Dome Fuji ice core, *Geophys. Res. Lett.*, 31, <https://doi.org/10.1029/2004GL021151>, 2004.

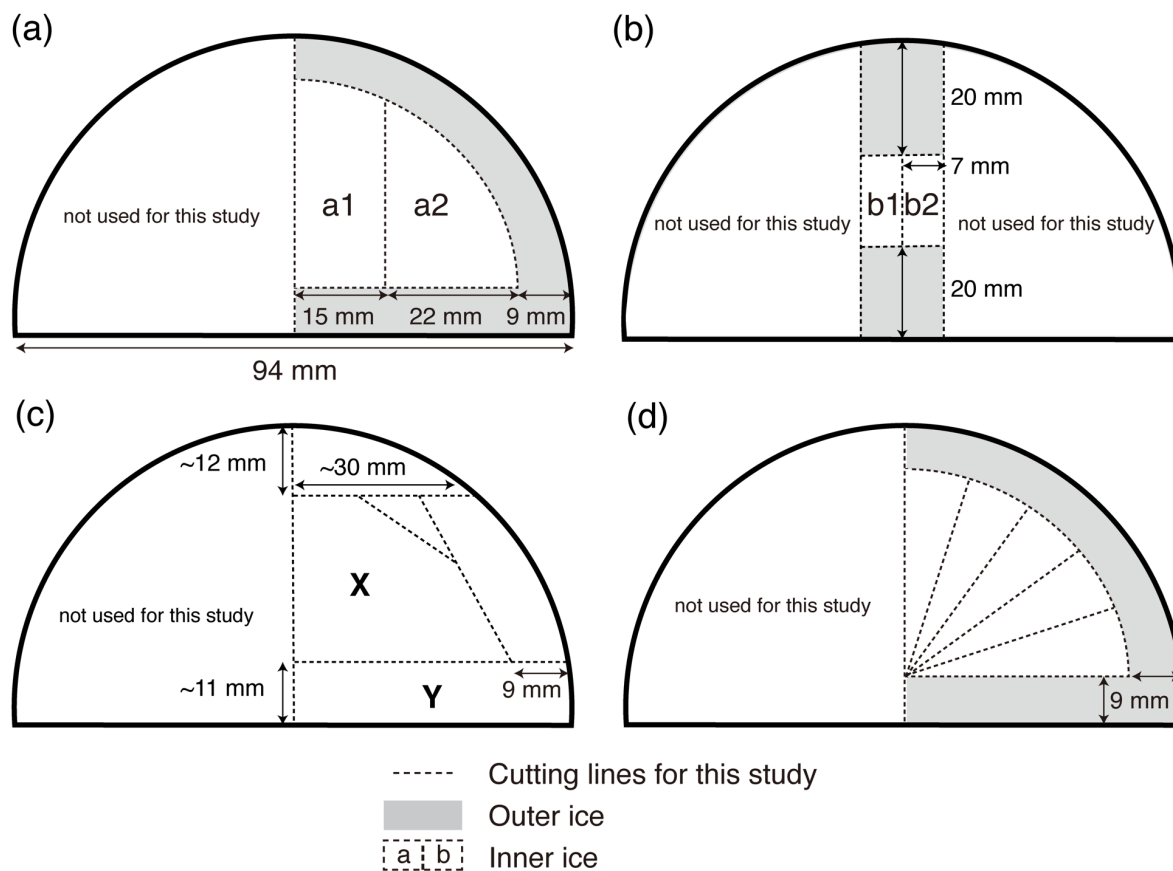


- Oyabu, I., Iizuka, Y., Uemura, R., Miyake, T., Hirabayashi, M., Motoyama, H., Sakurai, T., Suzuki, T., and Hondoh, T.: Chemical compositions of sulfate and chloride salts over the last termination reconstructed from the Dome Fuji ice core, inland Antarctica, *Journal of Geophysical Research: Atmospheres*, 119, 14045-14058, <https://doi.org/10.1002/2014JD022030>, 2014.
- 680 Oyabu, I., Kawamura, K., Kitamura, K., Dallmayr, R., Kitamura, A., Sawada, C., Severinghaus, J. P., Beaudette, R., Orsi, A., Sugawara, S., Ishidoya, S., Dahl-Jensen, D., Goto-Azuma, K., Aoki, S., and Nakazawa, T.: New technique for high-precision, simultaneous measurements of CH₄, N₂O and CO₂ concentrations, isotopic and elemental ratios of N₂, O₂ and Ar, and total air content in ice cores by wet extraction, *Atmos. Meas. Tech.*, 13, 6703-6731, <https://doi.org/10.5194/amt-13-6703-2020>, 2020.
- 685 Salamatin, A. N., Lipenkov, V., Ikeda-Fukazawa, T., and Hondoh, T.: Kinetics of air-hydrate nucleation in polar ice sheets, *J. Cryst. Growth*, 223, 285-305, [https://doi.org/10.1016/S0022-0248\(00\)01002-2](https://doi.org/10.1016/S0022-0248(00)01002-2), 2001.
- Seltzer, A. M., Buizert, C., Baggenstos, D., Brook, E. J., Ahn, J., Yang, J.-W., and Severinghaus, J. P.: Does $\delta^{18}\text{O}$ of O₂ record meridional shifts in tropical rainfall?, *Clim. Past*, 13, 1323-1338, <https://doi.org/10.5194/cp-13-1323-2017>, 2017.
- Severinghaus, J. P.: South Pole (SPICECORE) ¹⁵N, ¹⁸O, O₂/N₂ and Ar/N₂ (Version 1), U.S. Antarctic Program (USAP) Data Center [dataset], <https://doi.org/10.15784/601152>, 2019.
- 690 Severinghaus, J. P. and Battle, M. O.: Fractionation of gases in polar ice during bubble close-off: New constraints from firm air Ne, Kr and Xe observations, *Earth Planet. Sci. Lett.*, 244, 474-500, <https://doi.org/10.1016/j.epsl.2006.01.032>, 2006.
- Severinghaus, J. P., Beaudette, R., Headly, M. A., Taylor, K., and Brook, E. J.: Oxygen-18 of O₂ Records the Impact of Abrupt Climate Change on the Terrestrial Biosphere, *Science*, 324, 1431-1434, <https://doi.org/10.1126/science.1169473>, 2009.
- Shackleton, S., Bereiter, B., Baggenstos, D., Bauska, T. K., Brook, E. J., Marcott, S. A., and Severinghaus, J. P.: Is the Noble Gas-Based Rate of Ocean Warming During the Younger Dryas Overestimated?, *Geophys. Res. Lett.*, 46, 5928-5936, <https://doi.org/10.1029/2019GL082971>, 2019.
- 695 Sowers, T., Bender, M., and Raynaud, D.: Elemental and isotopic composition of occluded O₂ and N₂ in polar ice, *J. Geophys. Res.*, 94, 5137-5150, <https://doi.org/10.1029/JD094iD04p05137>, 1989.
- Suwa, M. and Bender, M. L.: Chronology of the Vostok ice core constrained by O₂/N₂ ratios of occluded air, and its implication for the Vostok climate records, *Quat. Sci. Rev.*, 27, 1093-1106, <https://doi.org/10.1016/j.quascirev.2008.02.017>, 2008a.
- 700 Suwa, M. and Bender, M. L.: O₂/N₂ ratios of occluded air in the GISP2 ice core, *Journal of Geophysical Research: Atmospheres*, 113, <https://doi.org/10.1029/2007JD009589>, 2008b.
- Watanabe, O., Jouzel, J., Johnsen, S., Parrenin, F., Shoji, H., and Yoshida, N.: Homogeneous climate variability across East Antarctica over the past three glacial cycles, *Nature*, 422, 509-512, <https://doi.org/10.1038/nature01525>, 2003.



Figures

710



715

Figure 1: Typical cross-sectional cutting plan. The outer black line in each panel is the original surface that was exposed to the atmosphere for ~20 years at -50 °C. Dotted lines are the cutting lines for this study. (a) Duplicate measurements and outer-inner comparisons. The sample length is 11 cm. For single (non-duplicate) measurements, only a2 is cut out. (b) Same as (a) but for 13 depths in 1000 – 1100 m with the sample length of 20 cm. (c) High-resolution analysis. Sections X and Y were used for the gas and ion measurements with the lengths of 2.5 and 1.25 cm, respectively. for X and Y, respectively. (d) Test of gas-loss under vacuum with the length of ~11 cm.

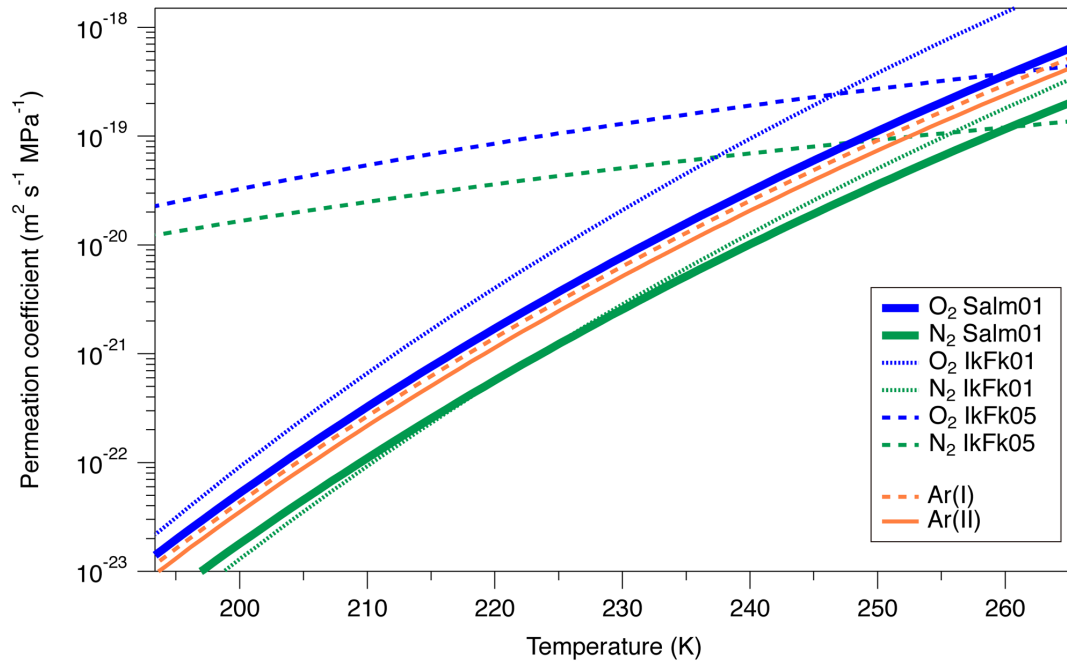
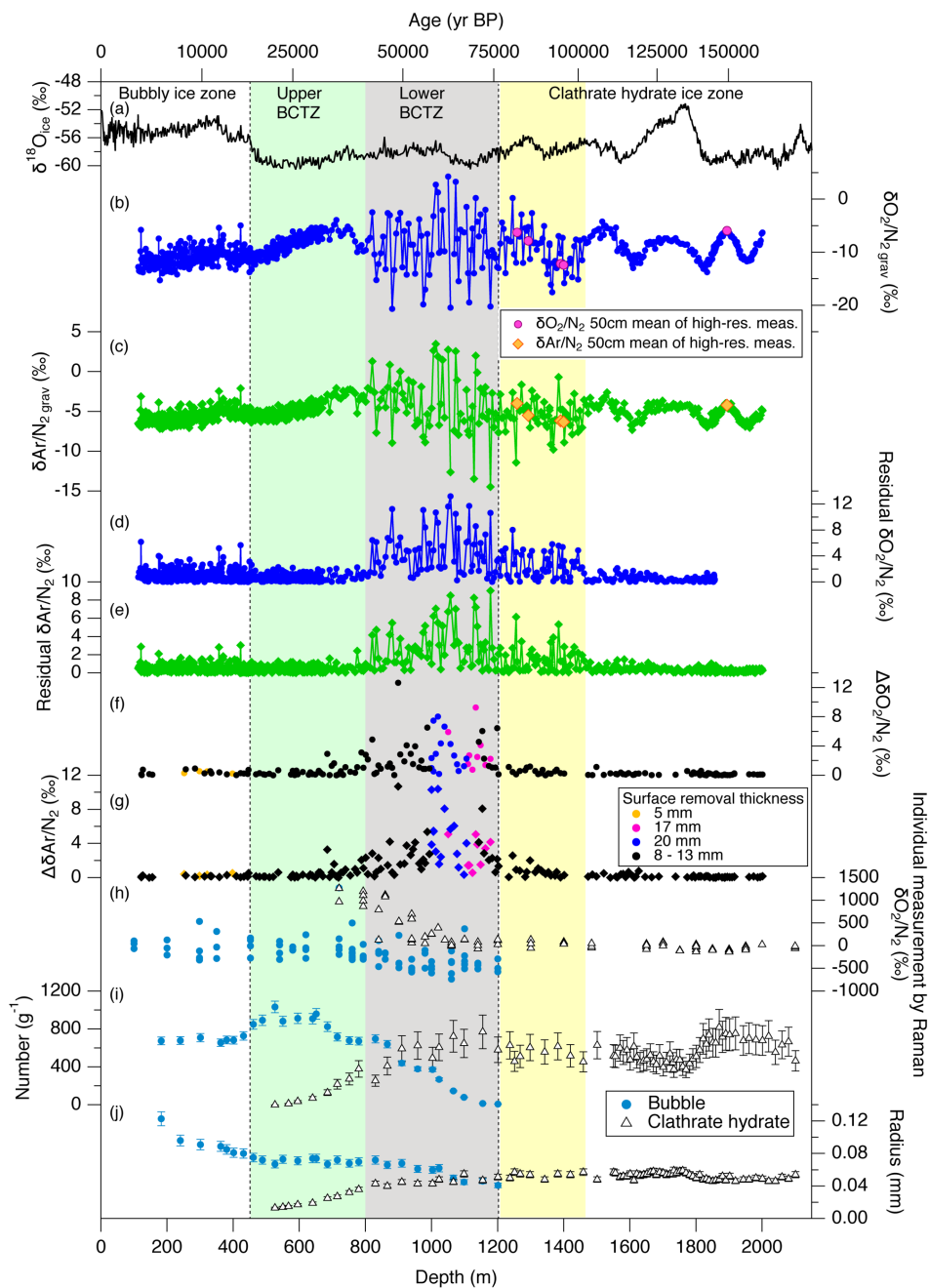


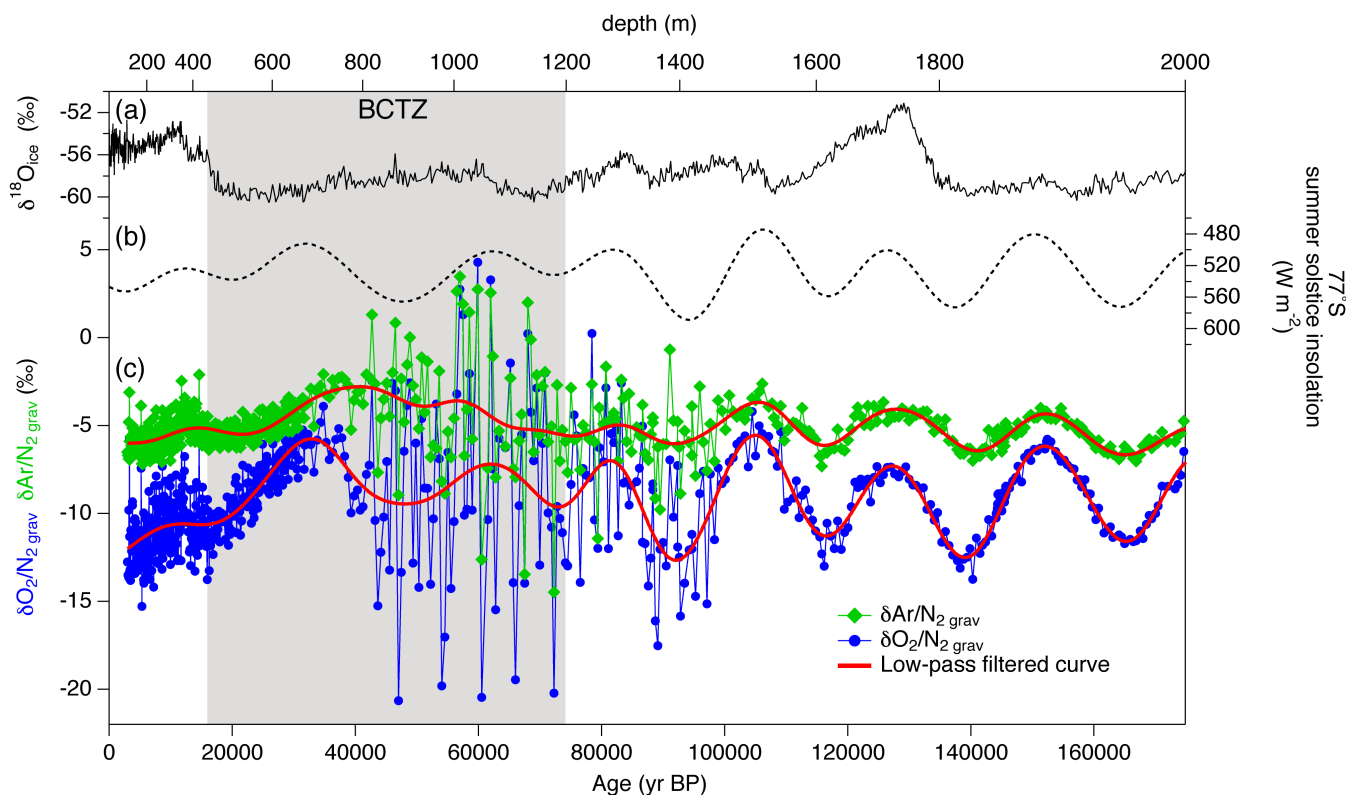
Figure 2: Permeation coefficients of O_2 , N_2 , Ar and air, estimated by different authors. See text for details.



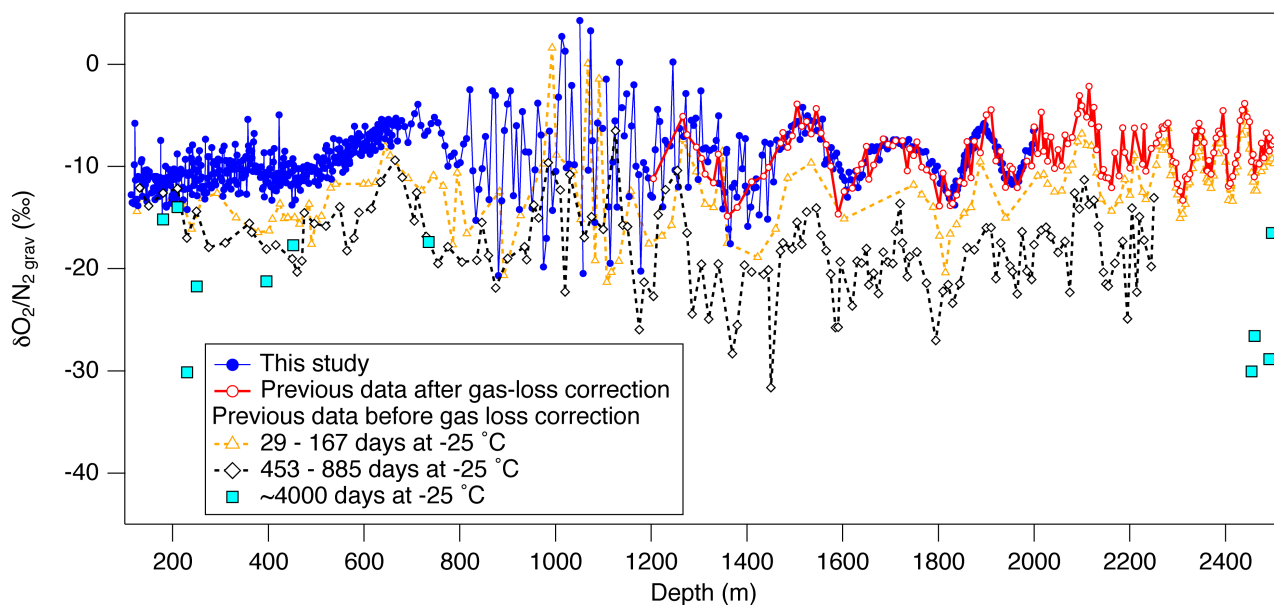
720

725

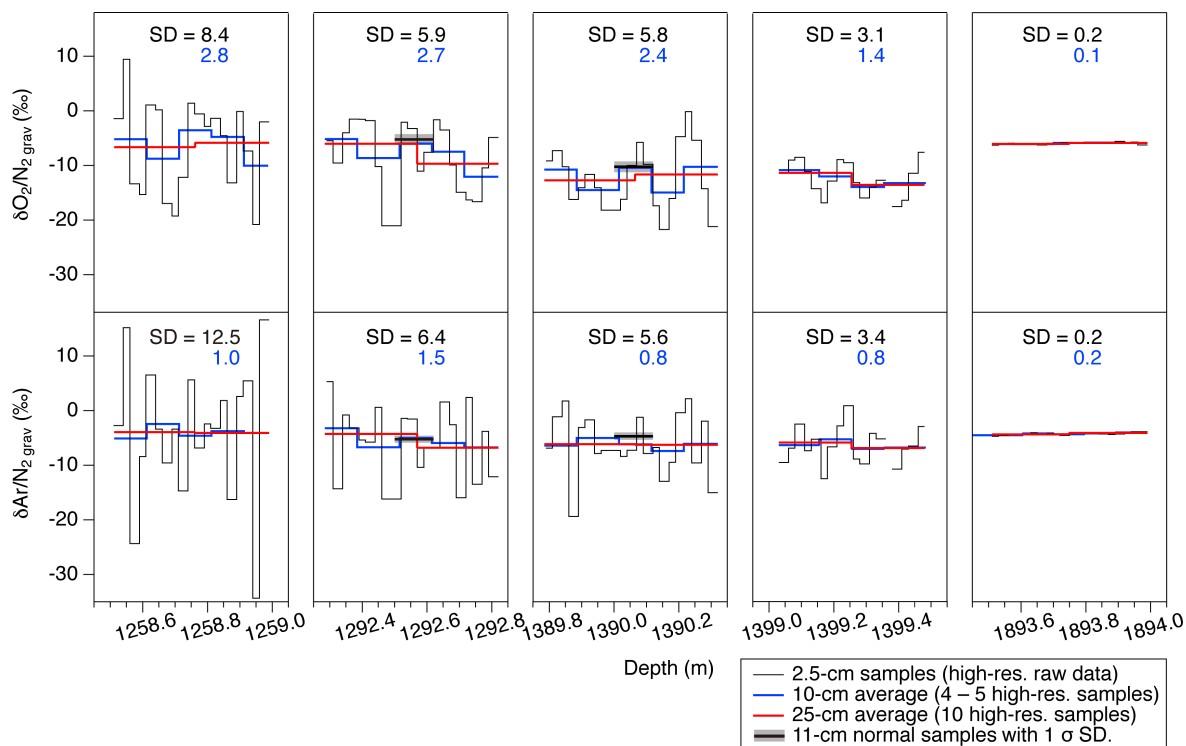
Figure 3: $\delta\text{O}_2/\text{N}_2$ and $\delta\text{Ar}/\text{N}_2$ records from the Dome Fuji ice core. Published data of water isotopes and air inclusions are also shown. (a) Stable water isotope record (Uemura et al., 2018), (b), (c) $\delta\text{O}_2/\text{N}_2$ and $\delta\text{Ar}/\text{N}_2$ after gravitational corrections, (d), (e) absolute residuals of $\delta\text{O}_2/\text{N}_2$ and $\delta\text{Ar}/\text{N}_2$ from their low-pass filtered curves, (f), (g) absolute pair differences of $\delta\text{O}_2/\text{N}_2$ and $\delta\text{Ar}/\text{N}_2$, (h) $\delta\text{O}_2/\text{N}_2$ in bubbles and clathrate hydrates observed by Raman spectroscopy (Ikeda-Fukazawa et al., 2001), and (i), (j) number concentrations and radius of bubbles and clathrate hydrates (Ohno et al., 2004).



730 **Figure 4:** $\delta\text{O}_2/\text{N}_2$ and $\delta\text{Ar}/\text{N}_2$ with published records plotted against the age of ice. (a) Stable water isotope record (Uemura et al., 2018), (b) summer solstice insolation at Dome Fuji (Laskar et al., 2004), and (c) $\delta\text{O}_2/\text{N}_2$ and $\delta\text{Ar}/\text{N}_2$ with low-pass filtered curves (cut-off at ~17 kyr, the filter was designed by Kawamura et al., 2007) (red lines).



735 **Figure 5:** Comparison of the new and previous $\delta\text{O}_2/\text{N}_2$ data from the Dome Fuji ice core. Solid circles (blue) are the new data (this study), and open circles (red) are the previous data corrected for gas loss during storage at $-25\text{ }^\circ\text{C}$ (Kawamura et al., 2007). Open triangles (orange), open diamonds (black), and solid square (light blue) are the uncorrected previous data for the storage period of 29 – 167 days, 453 – 885 days (Kawamura, 2001) and ~4000 days (11 years) (this study), respectively.



740

745

Figure 6: High-resolution data of $\delta\text{O}_2/\text{N}_2$ and $\delta\text{Ar}/\text{N}_2$ in 5 depth intervals. Black, blue and red lines are the raw data (2.5-cm resolution), 10-cm averages and 25-cm averages, respectively. Standard deviations (SD) of the raw 2.5-cm data (black) and 10-cm averages (blue) are shown in each panel. Thick horizontal black bars with gray shadings in some panels are the independent data from the 11-cm samples with 1σ error (measured by the standard protocol).

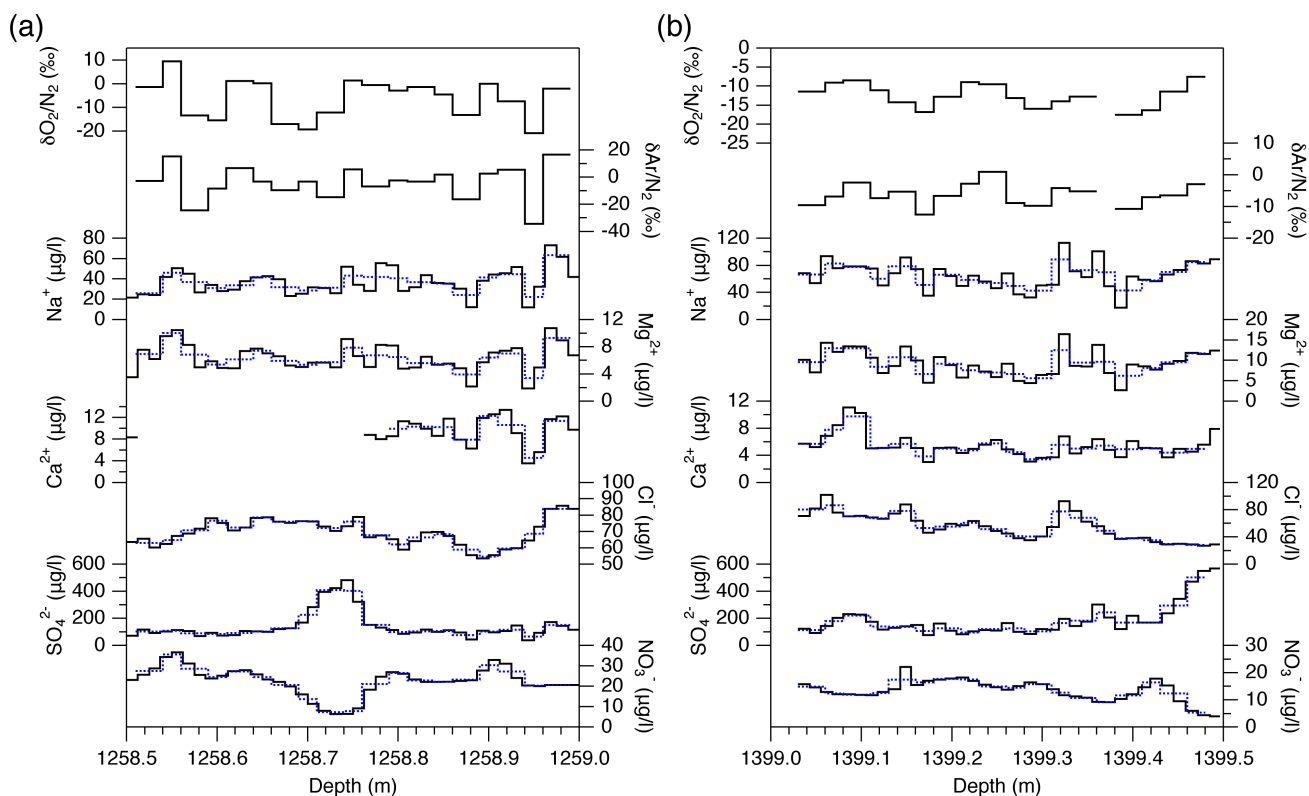


Figure 7: High-resolution data of $\delta O_2/N_2$ and $\delta Ar/N_2$ (2.5-cm resolution) and ion concentrations (1.25-cm resolution). Blue dotted lines are the interpolated ion data to match with the resolution of the gas data. The Ca^{2+} data for 1258.51 – 1258.75 m are excluded (high contamination due to sample handling error).

750

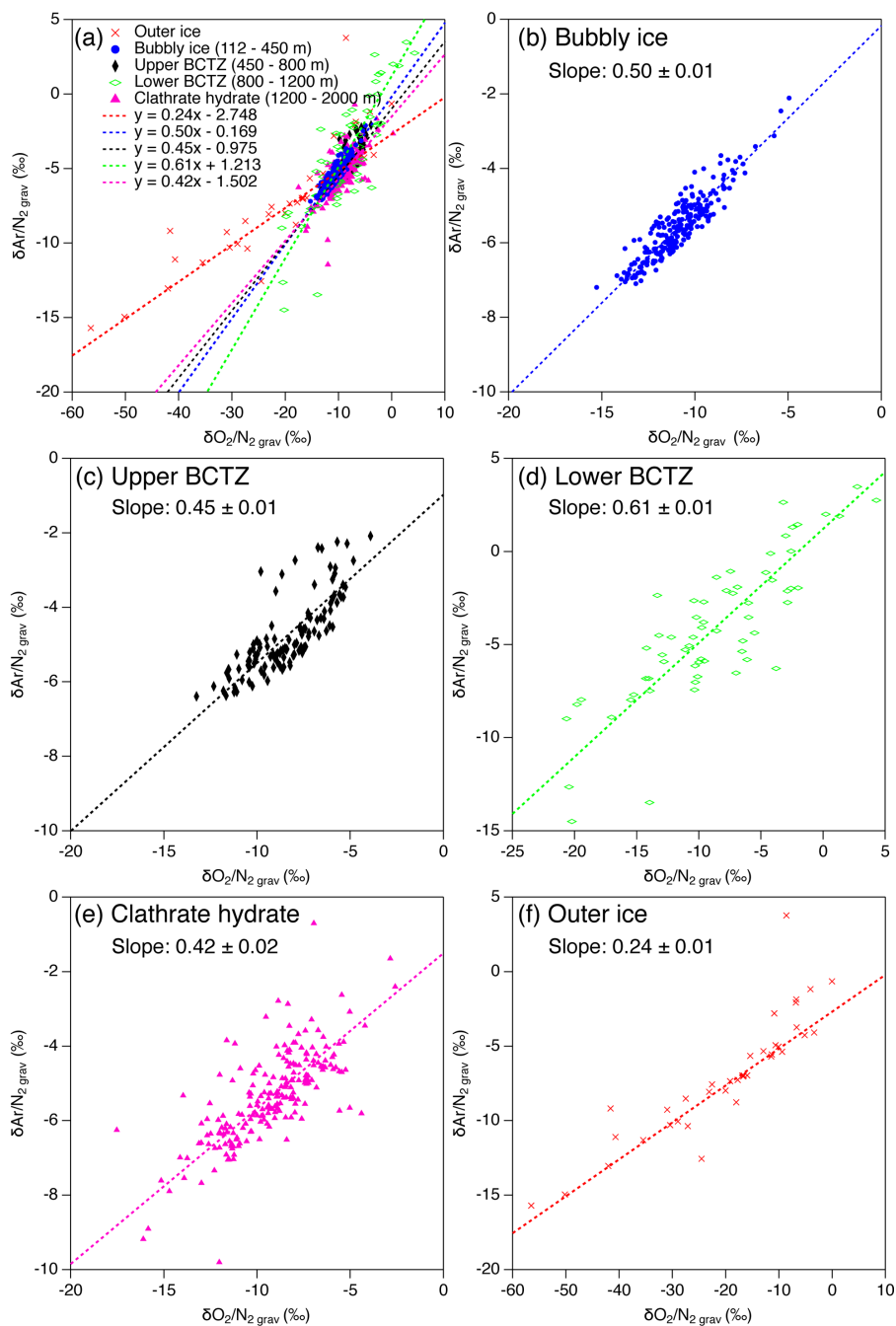


Figure 8: Scatter plot of $\delta\text{O}_2/\text{N}_2$ vs. $\delta\text{Ar}/\text{N}_2$ after gravitational correction using $\delta^{15}\text{N}$. (a) all data, (b) bubbly ice zone (112 – 450 m), (c) upper BCTZ (450 – 800 m), (d) lower BCTZ (800 – 1200 m), (e) clathrate hydrate ice zone (1200 – 2000 m), and (f) outer ice (bubbly ice and clathrate hydrate ice).

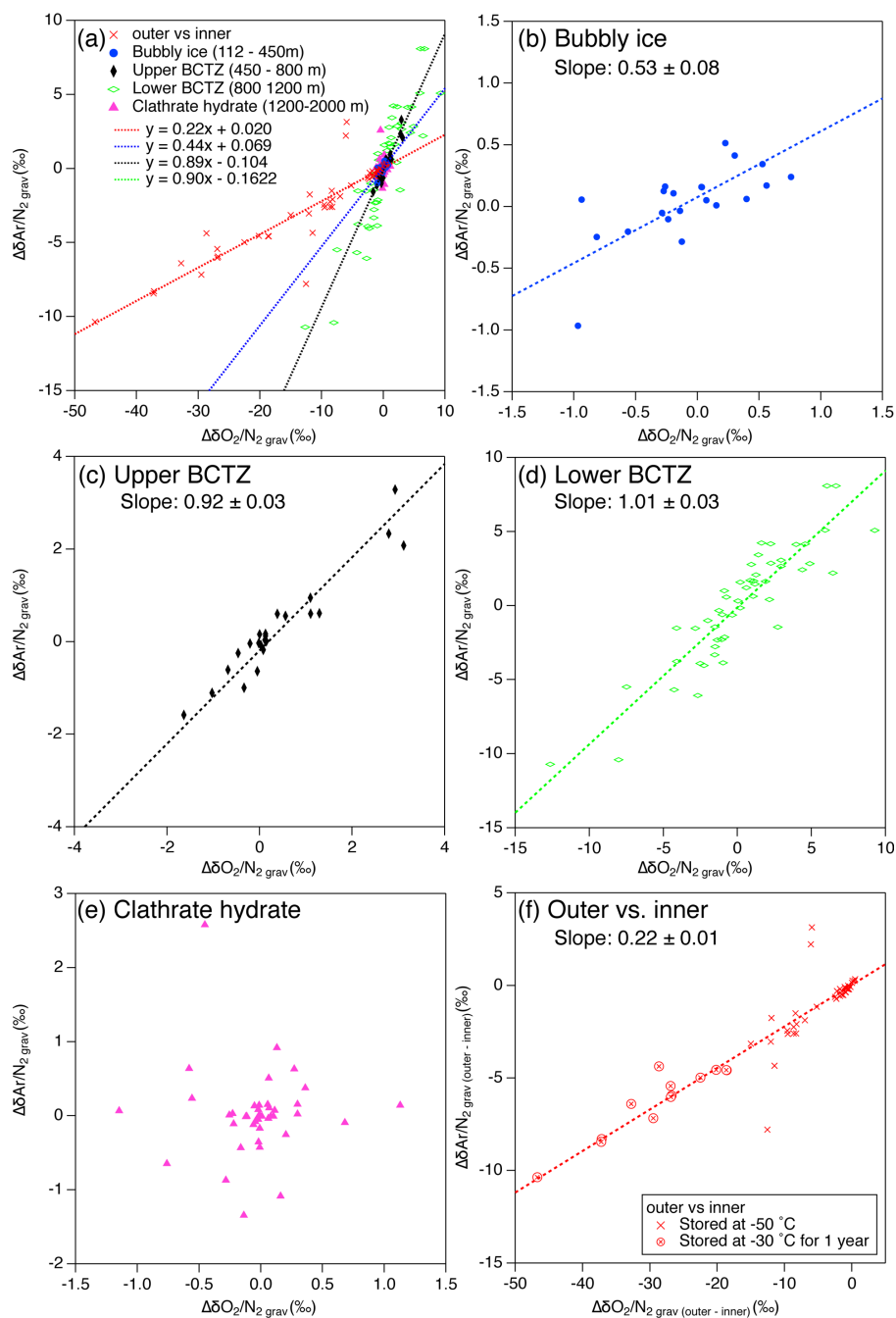


Figure 9: Scatter plot of pair differences of $\delta\text{O}_2/\text{N}_2$ and $\delta\text{Ar}/\text{N}_2$. (a) all data, (b) bubbly ice zone (112 – 450 m), (c) upper BCTZ (450 – 800 m), (d) lower BCTZ (800– 1200 m), (e) clathrate hydrate ice zone (1200 – 2000 m), and (f) pairs of outer and inner ice (bubbly ice and clathrate hydrate ice).

760

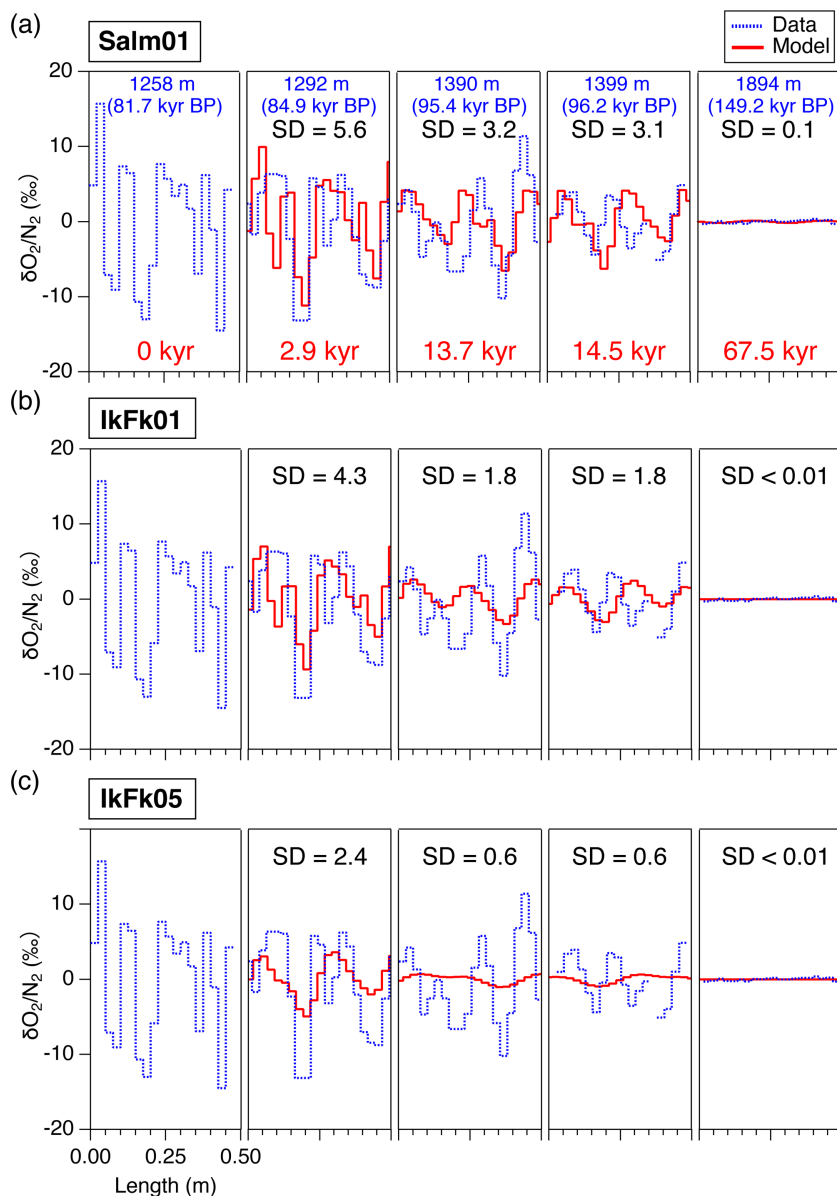


Figure 10: Comparison of the diffusion model outputs for $\delta O_2/N_2$ with different permeation parameters (red lines) and high-resolution data (blue dotted lines), at 1292 m, 1390 m, 1399 m and 1894 m. The data at 1258 m were given to the diffusion model as the initial condition. Solid lines (red) are the model outputs at the elapsed time of 2.9, 13.7, 14.5, 67.5 kyr, resampled at 2.5-cm intervals, to compare with the corresponding high-resolution data. Standard deviations (SD) of the model results are shown in each panel.

765

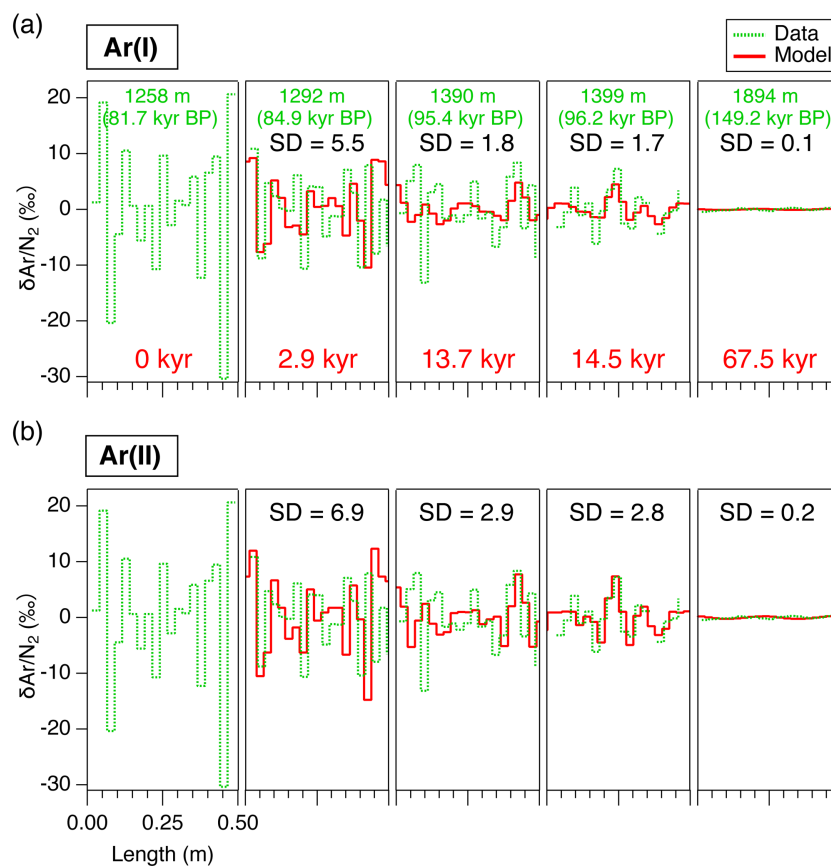
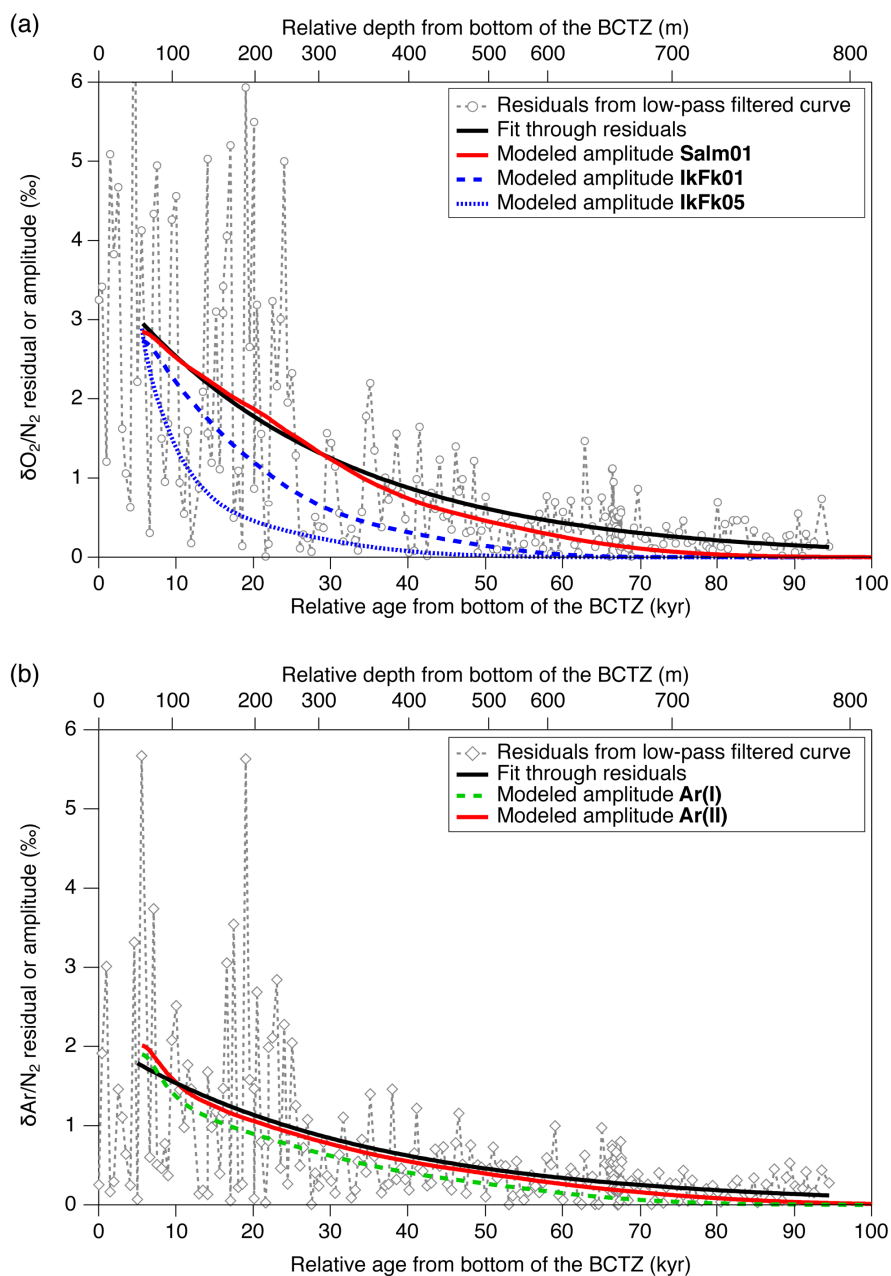


Figure 11: Same as Figure 10 but for $\delta\text{Ar}/\text{N}_2$.



770

Figure 12: Diffusive smoothing of (a) $\delta O_2/N_2$ and (b) $\delta Ar/N_2$ below the BCTZ. Open markers with dashed lines (gray) are the residuals from the low-pass filtered data. Black lines are exponential fits through the residuals for > 5600 years (corresponding to the model's initial age). The model results (standard deviations of 11-cm resampled outputs) with the best permeation parameters are shown by solid red lines. Blue and green lines are the other model results.

775



Tables

Table 1: Correlation coefficients between high-resolution gas data and ion concentrations within two 50-cm samples.

	$\delta\text{O}_2/\text{N}_2$	$\delta\text{Ar}/\text{N}_2$	Cl^-	SO_4^{2-}	NO_3^-	F^-	CH_3SO_3^-	Na^+	Mg^{2+}	Ca^{2+}	NH_4^+
1258.5 – 1259.0 m											
$\delta\text{O}_2/\text{N}_2$	1.00										
$\delta\text{Ar}/\text{N}_2$	0.75	1.00									
Cl^-	-0.18	0.07	1.00								
SO_4^{2-}	0.01	0.10	0.33	1.00							
NO_3^-	0.37	0.20	-0.49	-0.83	1.00						
F^-	0.47	0.37	-0.37	-0.46	0.78	1.00					
CH_3SO_3^-	0.62	0.51	-0.10	-0.43	0.67	0.52	1.00				
Na^+	0.61	0.71	0.24	0.10	0.15	0.39	0.60	1.00			
Mg^{2+}	0.72	0.74	0.21	0.16	0.26	0.58	0.60	0.82	1.00		
Ca^{2+}	(0.95)	(0.93)	(-0.04)	(0.77)	(0.56)	(0.37)	(0.83)	(0.75)	(0.78)	(1.00)	
NH_4^+	0.00	0.11	-0.54	-0.03	0.56	0.45	0.30	-0.02	0.05	0.14	1.00
1399.0 – 1399.5 m											
$\delta\text{O}_2/\text{N}_2$	1.00										
$\delta\text{Ar}/\text{N}_2$	0.70	1.00									
Cl^-	0.23	0.13	1.00								
SO_4^{2-}	0.43	0.30	-0.42	1.00							
NO_3^-	-0.40	-0.21	0.21	-0.83	1.00						
F^-	-0.03	-0.05	0.71	-0.52	0.40	1.00					
CH_3SO_3^-	-0.21	0.06	0.36	-0.24	0.36	0.47	1.00				
Na^+	0.53	0.48	0.47	0.52	-0.43	0.17	0.32	1.00			
Mg^{2+}	0.54	0.43	0.52	0.48	-0.42	0.26	0.29	0.96	1.00		
Ca^{2+}	0.52	0.44	0.55	0.12	-0.20	0.44	0.06	0.54	0.72	1.00	
NH_4^+	-0.06	0.00	-0.47	0.65	-0.71	-0.54	-0.32	0.13	0.06	-0.18	1.00

Bold numbers indicate significant correlations ($p < 0.05$). Numbers in brackets are calculated using the data from the lower 20 cm (because of the experimental problem in the Ca^{2+} data).